THE GEOLOGICAL SOCIETY OF AMERICA®

Secondary magnetic inclusions in detrital zircons from the Jack Hills, Western Australia, and implications for the origin of the geodynamo

Benjamin P. Weiss[1], Roger R. Fu[2], Joshua F. Einsle[3,4], David. R. Glenn[5,6], Pauli Kehayias[5,6], Elizabeth A. Bell[7], Jeff Gelb[8], Jefferson F.D.F. Araujo[1,9], Eduardo A. Lima[1], Cauê S. Borlina[1], Patrick Boehnke[10,11], Duncan N. Johnstone[4], T. Mark Harrison[7], Richard J. Harrison[3], and Ronald L. Walsworth[5, 6]

[1]Department of Earth, Atmospheric, and Planetary Sciences, Massachusetts Institute of Technology, Cambridge, Massachusetts 02139, USA
[2]Department of Earth and Planetary Sciences, Harvard University, Cambridge, Massachusetts 02138, USA
[3]Department of Earth Sciences, University of Cambridge, Cambridge CB2 3EQ, UK
[4]Department of Materials Science and Metallurgy, University of Cambridge, Cambridge CB3 0FS, UK
[5]Harvard-Smithsonian Center for Astrophysics, Cambridge, Massachusetts 02138, USA
[6]Department of Physics, Harvard University, Cambridge, Massachusetts 02138, USA
[7]Department of Earth, Planetary, and Space Sciences, University of California, Los Angeles, California 90095, USA
[8]Carl Zeiss X-ray Microscopy Inc., Pleasanton, California 94588, USA
[9]Department of Physics, Pontifical Catholic University of Rio de Janeiro, Rio de Janeiro 22451-900, Brazil
[10]Department of the Geological Sciences, University of Chicago, Chicago, Illinois 60637, USA
[11]Chicago Center for Cosmochemistry, Chicago, Illinois 60637, USA

ABSTRACT

The time of origin of Earth's dynamo is unknown. Detrital zircon crystals containing ferromagnetic inclusions from the Jack Hills of Western Australia have the potential to contain the oldest records of the geodynamo. It has recently been argued that magnetization in these zircons indicates that an active dynamo existed as far back as 4.2 Ga. However, the ages of ferromagnetic inclusions in the zircons are unknown. Here we present the first detailed characterization of the mineralogy and spatial distribution of ferromagnetic minerals in Jack Hills detrital zircons. We demonstrate that ferromagnetic minerals in most Jack Hills zircons are commonly located in cracks and on the zircons' exteriors. Hematite is observed to dominate the magnetization of many zircons, while other zircons also contain significant quantities of magnetite and goethite. This indicates that the magnetization of most zircons is likely to be dominantly carried by secondary minerals that could be hundreds of millions to billions of years younger than the zircons' crystallization ages. We conclude that the existence of the geodynamo prior to 3.5 Ga has yet to be established.

INTRODUCTION

The unknown early history of Earth's magnetic field has important implications for our understanding of the planet's thermal evolution and the process of dynamo generation. In particular, inner core crystallization, the likely power source for today's dynamo, is thought to have only initiated at <1.5 Ga (Davies et al., 2015). Therefore, identification of an early field would indicate that the core was stirred by other power sources, such as precipitation of Mg (O'Rourke and Stevenson, 2016), or perhaps that the dynamo was generated by exotic processes like a convecting basal magma ocean (Ziegler and Stegman, 2013). Furthermore, because Earth's field controls the penetration of the solar-wind electric field into the ionosphere, the dynamo's history may have strongly influenced Earth's water budget and oxidation state (Tarduno et al., 2014).

Although paleomagnetic studies of Archean rocks indicate that a dynamo with an intensity of at least half that of the present day existed by 3.45 Ga (Tarduno et al., 2014), the earlier history of the field is uncertain. With U-Pb ages ranging from ca. 3.0 Ga to 4.38 Ga (Holden et al., 2009), detrital zircon crystals from the Jack Hills of Western Australia have the potential to retain geodynamo records from the missing first billion years of Earth's history. Although zircon is itself not ferromagnetic, magnetization could be carried by ferromagnetic inclusions within the zircons (Fu et al., 2017; Sato et al., 2015).

It was recently proposed that the Jack Hills zircons contain records of the dynamo dating back to their oldest U-Pb crystallization ages of 4.2 Ga (Dare et al., 2016; Tarduno et al., 2015). However, it is currently unknown whether these zircons have escaped thermal and chemical remagnetization during the intervening time since their formation. In fact, many Jack Hills rocks were pervasively remagnetized sometime after 3.0 Ga (Weiss et al., 2015) (Appendix DR1 in the GSA Data Repository[1]). Although Tarduno et al. (2015) conducted a "micro-conglomerate test" in an attempt to demonstrate a lack of post-depositional remagnetization, this employed 0.5–0.8-mm-size specimens consisting predominantly of quartzite pebble material enclosing zircons with sizes of just 0.2–0.3 mm. As such, the result of their test rests on the unverified assumption that the magnetization of the specimens is dominated by inclusions within the embedded zircon. Furthermore, although Tarduno et al. (2015) and Bono et al. (2018) argued that thermal remagnetization of the zircons would have resulted in Pb/U variations during secondary ion mass spectrometry (SIMS) depth-profiling that they did not observe, their instrumentation should have been incapable of detecting such variations (Weiss et al., 2016). In any case, even if such variations could have been detected by Tarduno et al. (2015), such Pb/U depth-profiling is not a sensitive test for thermal remagnetization because of lead's extremely low diffusivity at 600 °C in non-metamict zircons under both dry and hydrous conditions (Cherniak and Watson, 2003).

[1]GSA Data Repository item 2018135, Figures DR1–DR12, Tables DR1–DR4, Movie DR1, and Appendices DR1–DR3, is available online at http://www.geosociety.org/datarepository/2018/ or on request from editing@geosociety.org.

Along with demonstrating a lack of thermal remagnetization, another key requirement for establishing that the bulk natural remanent magnetization (NRM) of a zircon crystal is a robust indicator of magnetic fields at the time of zircon crystallization is the demonstration that its ferromagnetic inclusions are dominantly primary rather than alteration products of primary inclusions or deposits in cracks and voids. Here we characterize the ferromagnetic mineral assemblage in Jack Hills zircons using compositional and magnetic analyses to assess whether magnetization in most Jack Hills zircons is carried dominantly by primary or secondary inclusions.

METHODS

We sought to identify the ferromagnetic mineralogy of the zircon inclusions, establish whether they are primary or secondary by focusing on their relationships to cracks and alteration textures, and test the efficacy of acid-washing for removing secondary inclusions. We conducted magnetic, compositional, and mineralogical analyses on 11 sets of Jack Hills detrital zircons (425 total zircons newly analyzed in this study, along with re-analysis of 2450 zircons previously studied by Bell et al. [2015]; Table DR1) from quartz pebble conglomerates sampled at the Erawandoo Hill Hadean-zircon discovery outcrop [site W74 of Weiss et al. (2016, their figure S2)]. Eleven sets of zircons were mounted in several different ways for our magnetic measurements (Appendix DR2). We mapped the three components of the isothermal remanent magnetization (IRM) and NRM fields above 381 zircons using quantum diamond microscopy (QDM) (Fu et al., 2017; Glenn et al., 2017) (Appendix DR2). QDM employs optically addressable nitrogen vacancy centers in diamond that are sensitive to magnetic fields via the Zeeman effect. We also mapped the vertical component of the NRM field of 109 zircons using superconducting quantum interference device (SQUID) microscopy (SM). SM enables ultra-sensitive measurements of net magnetic moments (Lima and Weiss, 2016; Fu et al. 2017). Curie temperatures of inclusions were estimated by SM mapping of thermal demagnetization of IRM.

Of the zircons imaged with QDM, 34 grains were subsequently analyzed with backscattered scanning electron microscopy (BSEM), energy dispersive spectroscopy (EDS), and wavelength dispersive spectroscopy (WDS). QDM is most sensitive to magnetic materials located up to tens of microns below the polished grain surfaces, while electron microscopy is only sensitive to the top <2 μm of the grains. Following these analyses, the three-dimensional Fe inclusion distribution in one zircon was then imaged using X-ray tomography using Carl Zeiss Xradia 520 Versa and Ultra XRM-L200 microscopes (spatial resolutions of 750 and 150 nm, respectively).

RESULTS

Zircons Not Treated with Concentrated Acid

We begin by discussing zircons not washed with acid and those washed with weak (0.5 N) HCl (Table DR1). SM measurements show that non-acid-washed zircons from set 4 have a mean NRM of 8.3×10^{-13} Am^2, 23% of which are $>1 \times 10^{-12}$ Am^2 (Fig. DR10A; Table DR3). QDM imaging of non-acid-washed zircons from set 1 carrying IRM (Fig. DR3) and set 3 carrying NRM (Figs. DR4A–DR4D) was conducted in a lower-sensitivity reconnaissance (261 zircons) mode followed by higher-sensitivity imaging (84 zircons) (see Glenn et al. [2017] and Table DR2). Of the 147 and 76 such zircons detected in the reconnaissance and higher-sensitivity modes, respectively, 122 (83%) and 55 (72%) respectively, exhibited magnetic anomalies centered on locations that are within ~20 μm of the grains' exteriors (Figs. 1A–1C; Figs. DR1A–DR1J). We observed similar results for zircons washed with 0.5 N HCl (i.e., sets 5 and 6): 67% of the 9 zircons detected with QDM showed exterior-only NRM (bottom grains in Figs. DR4E and DR4J; and both grains in Figs. DR4G and DR4I). Of the 23 non-acid-washed and 0.5 N HCl-washed zircons analyzed with WDS, 91% (including 93% of the 15 zircons with exterior-only magnetic sources) have secondary Fe-rich rinds located within <5 μm of the grain exteriors (Figs. 1A–1C; Figs. DR1A, DR1B, DR1D–DR1J, DR2, DR5, and DR6). These rinds have thicknesses ranging from <2 μm for most zircons (e.g., Figs. 1B–1D) and up to 10 μm for one zircon (e.g., Fig. DR1). Additionally, X-ray tomography of an uncracked, optically clear Hadean zircon with exterior-only magnetic sources, which showed no sign of secondary mineralization based on optical inspection, identified high-X-ray absorption grains (consistent with Fe-rich materials) exclusively on the zircon exterior (Fig. 2). The spatial association of magnetic anomalies and Fe-rich secondary materials suggests that the latter carry most of the magnetization in these zircons. Although some exterior magnetic anomalies are not associated with Fe-rich materials detectable with WDS (e.g., anomaly at upper right of grain in Figure 1B), the difference

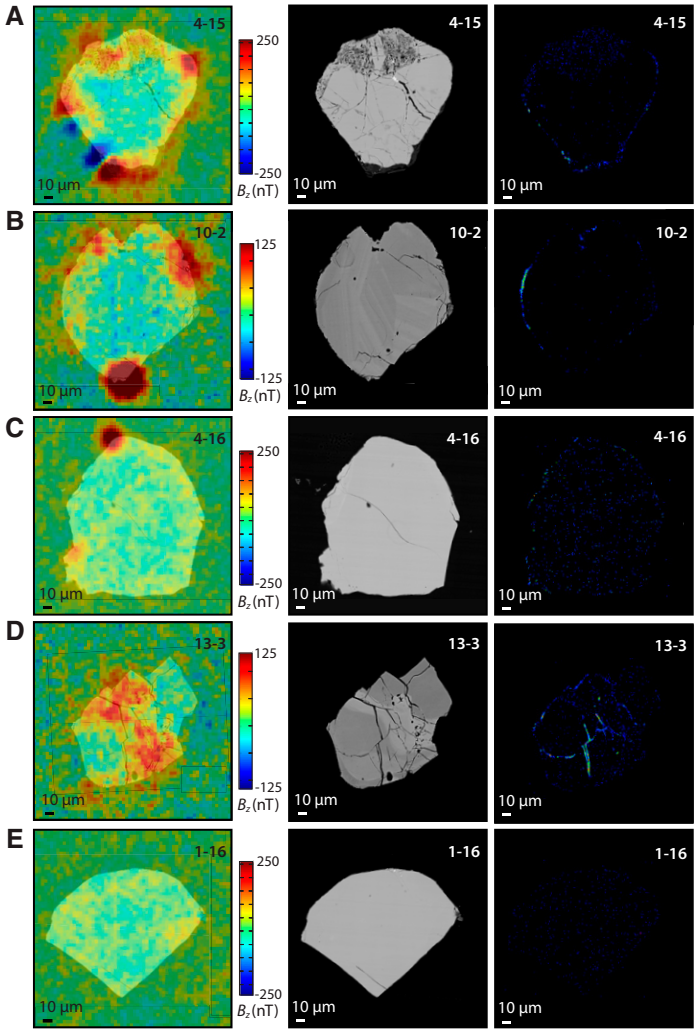

Figure 1. Magnetization, texture, and composition of Jack Hills (Western Australia) zircons not washed with acid (i.e., set 1). Shown are quantum diamond microscopy (QDM) maps of the vertical component of the magnetic field at ~1–10 μm above the samples overlain on backscattered electron microscopy (BSEM) images (left), BSEM images (middle), and maps of Fe abundance from wavelength dispersive spectroscopy (WDS) (right). A: Zircon RSES 199–4–15 (RSES—Australian National University Research School of Earth Sciences) (Pb-Pb age of <3900 Ma). B: Zircon RSES 199–10–2 (Pb-Pb age of 4050 ± 8 Ma). C: Zircon RSES 199–4–16 (Pb-Pb age of 3973 ± 8 Ma). D: Zircon RSES 199–13–3 (Pb-Pb age <3900 Ma). E: Zircon RSES 199–1–16 (Pb-Pb age <3900 Ma). See Figures DR1 and DR2 (see footnote 1) for more QDM and BSEM analyses of set 1 zircons, and see Figure DR3 for QDM data on all set 1 zircons. See Table DR4 for the Pb-Pb ages of these zircons.

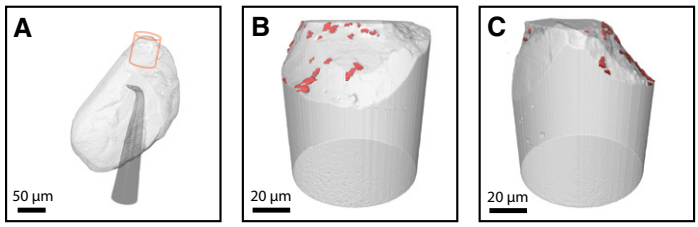

Figure 2. X-ray tomography of a Jack Hills (Western Australia) zircon not washed with acid (i.e., set 1). Shown is zircon RSES 199–1–15 (RSES—Australian National University Research School of Earth Sciences), which has a U-Pb age of 4019 ± 5 Ma. A: Tomogram from Xradia 520 Versa showing entire grain (light gray) on mount (dark hook). Cylinder shows location of tomograms in B and C. B, C: Orthogonal views from Ultra XRML200 microscope. Red voxels have high X-ray absorption relative to that of zircon host (gray) and are inferred to be Fe-rich particles. See Movie DR1 (see footnote 1) for renderings of these data from other viewpoints, and Fig. DR3C for maps of this zircon's magnetic field.

in depth sensitivity between these techniques (see Methods) implies that many of these anomalies may be likely associated with secondary Fe-rich materials located >2 µm beneath the polished grain surfaces.

We found that just 21% of detected zircons not washed with strong HCl contain interior magnetic sources (i.e., that lie deeper than 20 µm from the rim) (e.g., Fig. 1D; Figs. DR1M–DR1P; Table DR2). Although the bulk magnetizations of the latter zircons are better candidates for being dominantly carried by primary ferromagnetic materials, the exteriors of many of these zircons nevertheless carry substantial magnetization (e.g., Fig. 1D; Figs. DR1M–DR1P). In particular, 100% (5 out of 5) these zircons with interior magnetic sources analyzed with electron microscopy have Fe-rich rinds (e.g., Fig. 1D; Figs. DR1M, DR1O, and DR1P). Furthermore, we found that 100% (5 out of 5) of these zircons analyzed with electron microscopy host Fe-rich secondary minerals in interior cracks and metamict zones (e.g., Fig. 1D; Figs. DR1M, DR1O, and DR1P). QDM maps of the zircon host conglomerate found that the IRM of *in situ* zircons is significantly weaker than that associated with quartz grain boundaries that are commonly filled with Fe oxides (Fig. DR7). Therefore, until it is demonstrated that the NRMs of the Tarduno et al. (2015) micro-conglomerate test samples are dominated by primary inclusions in the zircon rather than by the surrounding rock, the outcome of that test should be regarded as uncertain.

Raman spectroscopy indicates the presence of hematite in at least two zircons prior to any lab heating (Fig. DR8). Furthermore, SM measurements of thermal demagnetization of IRM (Fig. 3; Fig. DR9), found that 100% of 9 grains with clearly identified Curie temperatures contained hematite (Curie temperature 675 °C) while 22% also contained magnetite (Curie temperature 580 °C). These data also demonstrate that several zircons likely contain goethite (Curie temperatures 50–120 °C) and possibly pyrrhotite (Curie temperature 325 °C). During repeat heating experiments, it was observed that a zircon dominated by hematite during the first heating became dominated by magnetite during the second heating, indicating that heating severely altered the magnetization carriers (Fig. DR9C).

These observations collectively indicate that the NRM and IRM in most of our Jack Hills zircons not washed with concentrated HCl are predominantly carried by secondary Fe oxides deposited on the zircon exterior or within cracks and voids in the zircon interior. Our identification of hematite as a major remanence carrier contrasts with the observations of Tarduno et al. (2015), who found that essentially all of their analyzed zircons had remanence apparently dominated by magnetite. A possible explanation for this discrepancy is that hematite was originally present in the zircons of Tarduno et al. (2015), but was altered to magnetite by their heating experiments (e.g., Fig. DR9C) prior to their lowest-temperature checks for alteration (i.e., 550 °C).

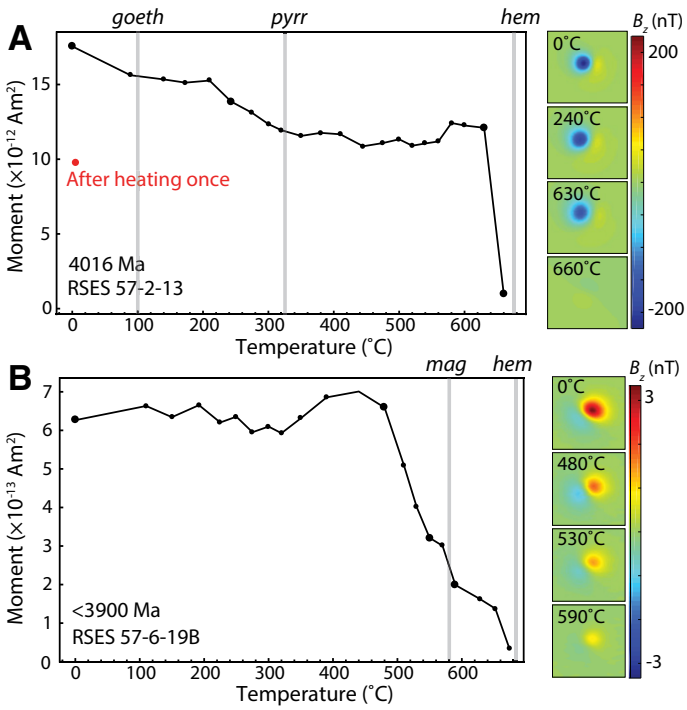

Figure 3. Thermal demagnetization of non-acid-washed Jack Hills (Western Australia) zircons carrying isothermal remanent magnetization (IRM) (i.e., set 2). Shown is the moment inferred from SQUID microscopy (SM) maps following each thermal demagnetization step (0 °C denotes no heating). Red point indicates a second IRM experiment conducted after the zircon had been heated to 680 °C. At right of each demagnetization curve are SM maps for selected demagnetization steps (large black circles). SM maps show the vertical component of the magnetic field ~230 µm above the zircons. Both zircons were found to contain origin-trending, single-component IRMs. A: Zircon RSES 57–2–13 (RSES—Australian National University Research School of Earth Sciences) (Pb-Pb age 4016 ± 6 Ma). See Figure DR8 (see footnote 1) for Raman spectrum of this zircon, taken prior to laboratory heating, that identifies hematite. B: Fragment of zircon RSES 57–6–19 (Pb-Pb age <3900 Ma). See Figure DR9 for thermal demagnetization data of more Jack Hills zircons, including a second fragment from zircon in B.

Zircons Treated with Concentrated (6N) Acid

SM measurements of set 9 find that zircons washed in concentrated HCl have a mean NRM only 59% of that of non-acid-washed zircons (Fig. DR10B; Table DR3). Furthermore, only 12% of acid-washed zircons have moments >1 × 10^{-12} Am^2. QDM measurements of sets 7 and 8 show that IRM is also weakened by acid-washing, with only 58% of such zircons detected (compared to 90% of unwashed set 1 zircons analyzed with QDM in the high-sensitivity mode).

Even so, QDM imaging showed that of the 14 zircons with detectable IRM, 29% still have magnetic sources confined largely to their exteriors (Fig. 4C; Fig. DR12A [both grains], and DR12C [bottom grain]). Furthermore, 36% of the 11 grains analyzed with EDS still have Fe-rich exterior rinds (Figs. 4B and 4C; Figs. DR11E and DR11H). Also, 100% of the 8 zircons analyzed with EDS and having interior magnetic sources contain Fe-rich cracks and alteration textures in their interiors (Figs. 4A and 4B; Figs. DR11A, DR11C–DR11G). Again, we cannot exclude the possibility that interior anomalies not associated with Fe-rich surface alteration visible in electron microscopy are instead associated with such alteration minerals below the polished surface. Overall, our analyses demonstrate that washing with concentrated HCl reduces the NRM and IRM of the zircons, particularly on the grain exteriors. Unfortunately, this often still leaves large quantities of Fe-rich alteration materials behind that could carry significant remanence. As described in Appendix DR3, these results are broadly consistent with the observations of Fe oxide inclusions by Bell et al. (2015).

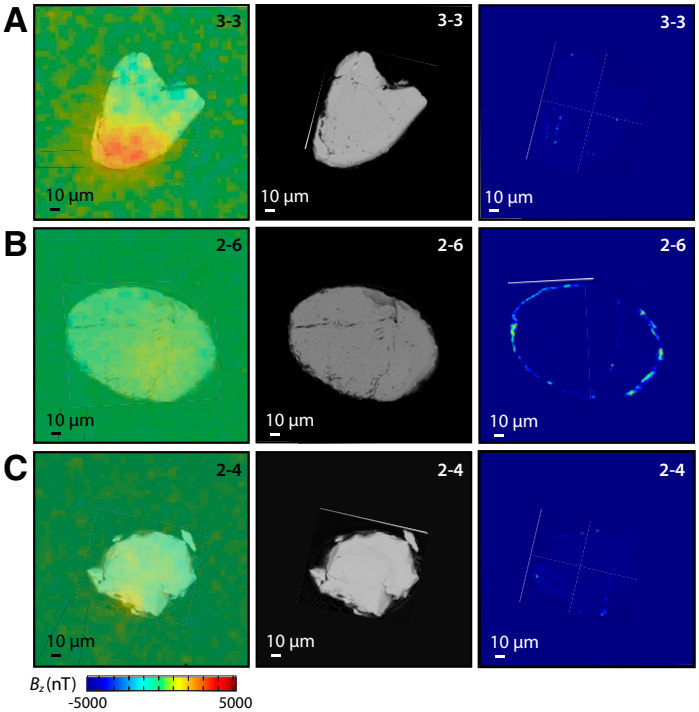

Figure 4. Magnetization, texture and composition of Jack Hills (Western Australia) zircons washed with 6 N HCl for 12 min (i.e., set 7) and 1 h (i.e., set 8). Shown are quantum diamond microscopy (QDM) maps of the vertical component of the magnetic field at ~1–10 µm above the samples overlain on backscattered electron microscopy (BSEM) images (left), BSEM images (middle), and maps of Fe abundance from energy dispersive spectroscopy (EDS) (right). A: Zircon D175M-B1–3–3. B: Zircon D175M-B2–2–6. C: Zircon D175M-B2–2–4. See Figures DR11–DR12 (see footnote 1) for measurements of additional acid-washed zircons.

CONCLUSIONS

Collectively, our analyses indicate that most Jack Hills zircons not washed with concentrated HCl have NRM and IRM likely dominantly carried by secondary iron oxides, some of which are hematite. In particular, of 85 such zircons detected by QDM in its high-resolution mode, 72% have magnetic anomalies only observed at the exterior of the grains. All such zircons analyzed with electron microscopy were found to have Fe-rich secondary rinds. Furthermore, even the few zircons with interior magnetic sources were found to have spatially associated cracks containing Fe-rich alteration products. These minerals were apparently deposited on the zircons' exteriors or within voids in the zircons' interiors at an unknown time(s) over the past 3–4 b.y. since the zircons formed. Such alteration may have coincided with known thermal disturbances and/or aqueous alteration events at ca. 2.6, ca. 2.0, ca. 1.8, ca. 1.2, ca. 1.1, and ca. 0.8 Ga (summarized in Weiss et al., 2015), and/or during deep weathering over the past ~0.2 b.y. (Pidgeon et al., 2017). Consistent with this, nearly all monazite and xenotime inclusions in Jack Hills zircons, including those apparently entirely enclosed within uncracked regions, have U-Pb ages younger than 2.6 Ga, indicating they formed long after the zircons crystallized (Rasmussen et al., 2011). The state of Jack Hills zircon ferromagnetic inclusions differs greatly from that in 0.767 ka non-detrital zircons from the Bishop Tuff, which commonly are in the form of primary magnetite grains that dominate the stable NRM (Fu et al., 2017). We conclude that the ages of NRMs in previously studied Jack Hills zircons are unknown. As such, there currently is no robust evidence for a geodynamo active prior to the oldest known well-preserved rock record at 3.5 Ga.

ACKNOWLEDGMENTS

These analyses were supported by National Science Foundation grant EAR1647504, Thomas F. Peterson, Jr., and a Chamberlin Postdoctoral Fellowship to Boehnke. We thank A. Steele for use of his Raman microscope and N. Chatterjee for assistance with the microprobe.

REFERENCES CITED

Bell, E.A., Boehnke, P., Hopkins-Wielicki, M.D., and Harrison, T.M., 2015, Distinguishing primary and secondary inclusion assemblages in Jack Hills zircons: Lithos, v. 234–235, p. 15–26, https://doi.org/10.1016/j.lithos.2015.07.014.

Bono, R.K., Tarduno, J.A., Dare, M.S., Mitra, R.D., and Cottrell, R.D., 2018, Cluster analysis on a sphere: Application to magnetizations from metasediments of the Jack Hills, Western Australia: Earth and Planetary Science Letters, v. 484, p. 67–80, https://doi.org/10.1016/j.epsl.2017.12.007.

Cherniak, D.J., and Watson, E.B., 2003, Diffusion in zircon: Reviews in Mineralogy and Geochemistry, v. 53, p. 113–143, https://doi.org/10.2113/0530113.

Dare, M.S., Tarduno, J.A., Bono, R.K., Cottrell, R.D., Beard, J.S., and Kodama, K.P., 2016, Detrital magnetite and chromite in Jack Hills quartzite cobbles: Further evidence for the preservation of primary magnetizations and new insights into sediment provenance: Earth and Planetary Science Letters, v. 451, p. 298–314, https://doi.org/10.1016/j.epsl.2016.05.009.

Davies, C., Pozzo, M., Gubbins, D., and Alfè, D., 2015, Constraints from material properties on the dynamics and evolution of Earth's core: Nature Geoscience, v. 8, p. 678–685, https://doi.org/10.1038/ngeo2492.

Fu, R.R., et al., 2017, Evaluating the paleomagnetic potential of single zircon crystals using the Bishop Tuff: Earth and Planetary Science Letters, v. 458, p. 1–13, https://doi.org/10.1016/j.epsl.2016.09.038.

Glenn, D.R., Fu, R.R., Kehayias, P., Le Sage, D., Lima, E.A., Weiss, B.P., and Walsworth, R.L., 2017, Micrometer-scale magnetic imaging of geological samples using a quantum diamond microscope: Geochemistry Geophysics Geosystems, v. 18, https://doi.org/10.1002/2017GC006946.

Holden, P., Lanc, P., Ireland, T.R., Harrison, T.M., Foster, J.J., and Bruce, Z., 2009, Mass-spectrometric mining of Hadean zircons by automated SHRIMP multi-collector and single-collector U/Pb zircon age dating: The first 100,000 grains: International Journal of Mass Spectrometry, v. 286, p. 53–63, https://doi.org/10.1016/j.ijms.2009.06.007.

Lima, E.A., and Weiss, B.P., 2016, Ultra-high sensitivity moment magnetometry of geological samples using magnetic microscopy: Geochemistry Geophysics Geosystems, v. 17, https://doi.org/10.1002/2016GC006487.

O'Rourke, J.G., and Stevenson, D.J., 2016, Powering Earth's dynamo with magnesium precipitation from the core: Nature, v. 529, p. 387–389, https://doi.org/10.1038/nature16495.

Pidgeon, R.T., Nemchin, A.A., and Whitehouse, M.J., 2017, The effect of weathering on U–Th–Pb and oxygen isotope systems of ancient zircons from the Jack Hills, Western Australia: Geochimica et Cosmochimica Acta, v. 197, p. 142–166, https://doi.org/10.1016/j.gca.2016.10.005.

Rasmussen, B., Fletcher, I.R., Muhling, J.R., Gregory, C.J., and Wilde, S.A., 2011, Metamorphic replacement of mineral inclusions in detrital zircon from Jack Hills, Australia: Implications for the Hadean Earth: Geology, v. 39, p. 1143–1146, https://doi.org/10.1130/G32554.1.

Sato, M., Yamamoto, S., Yamamoto, Y., Okada, Y., Ohno, M., Tsunakawa, H., and Maruyama, S., 2015, Rock-magnetic properties of single zircon crystals sampled from the Tanzawa tonalitic pluton, central Japan: Earth, Planets, Space, v. 67, p. https://doi.org/10.1186/s40623-40015-40317-40629.

Tarduno, J.A., Blackman, E.G., and Mamajek, E.E., 2014, Detecting the oldest geodynamo and attendant shielding from the solar wind: Implications for habitability: Physics of the Earth and Planetary Interiors, v. 233, p. 68–87, https://doi.org/10.1016/j.pepi.2014.05.007.

Tarduno, J.A., Cottrell, R.D., Davis, W.J., Nimmo, F., and Bono, R.K., 2015, A Hadean to Paleoarchean geodynamo recorded by single zircon crystals: Science, v. 349, p. 521–524, https://doi.org/10.1126/science.aaa9114.

Weiss, B.P., Maloof, A.C., Harrison, T.M., Swanson-Hysell, N.L., Fu, R.R., Kirschvink, J.L., Watson, E.B., Coe, R.S., Tikoo, S.M., and Ramezani, J., 2016, Reply to Comment on: "Pervasive remagnetization of detrital zircon host rocks in the Jack Hills, Western Australia and implications for records of the early dynamo": Earth and Planetary Science Letters, v. 450, p. 409–412, https://doi.org/10.1016/j.epsl.2016.07.001.

Weiss, B.P., et al., 2015, Pervasive remagnetization of detrital zircon host rocks in the Jack Hills, Western Australia and implications for records of the early geodynamo: Earth and Planetary Science Letters, v. 430, p. 115–128, https://doi.org/10.1016/j.epsl.2015.07.067.

Ziegler, L. B., and Stegman, D. R., 2013, Implications of a long-lived basal magma ocean in generating Earth's ancient magnetic field: Geochemistry Geophysics Geosystems, v. 14, https://doi.org/10.1002/2013GC005001.

Manuscript received 27 November 2017
Revised manuscript received 13 February 2018
Manuscript accepted 15 February 2018

Printed in USA

GSA Data Repository item 2018135
Appendices DR1-3, Figures DR1-13, Tables DR1-4, and Movie DR1

Supplementary Materials for: B. P. Weiss et al. (2018) Secondary magnetic inclusions in detrital zircons from the Jack Hills, Western Australia and implications for the origin of the geodynamo

Appendix DR1. Paleomagnetism of Jack Hills Rocks

The present study focuses on the remagnetization history of the zircons over the last 4.4 billion years. This goes beyond our previous Jack Hills studies (Weiss et al. 2015; 2016), which examined whether the host rocks for Jack Hills zircons have been remagnetized since deposition at 3.0 Ga. Weiss et al. (2015; 2016) provided evidence that the Jack Hills rocks in the vicinity of the Hadean-zircon discovery outcrop at Erawandoo Hill have been pervasively remagnetized up to peak unblocking temperatures of 320-500°C. They inferred this from 12 baked contact, fold, and conglomerate tests, all of which either failed or were inconclusive. These tests included 3 conglomerate tests on several cm-diameter cobbles from outcrops located several hundred meters northwest and northeast of Erawandoo Hill. These results contrast with a positive cobble conglomerate test conducted at the University of Rochester by Tarduno and Cottrell (2013) and recently augmented with new measurements by Dare et al. (2016) and Bono et al. (2018). Unlike Tarduno and Cottrell (2013), who observed stable NRM unblocking up to the 580°C Curie point of magnetite in most samples, nearly all of the cobbles in Weiss et al. (2015) [as well as cobbles measured at Lehigh University that are reported in Dare et al. (2016); see their Figs. 8b, 9b, S13b, and S14b], show little evidence of stable, origin-trending NRM blocked above the 350°C except when it is apparently carried by hematite or maghemite. The differences between the data acquired at MIT and Lehigh with those from Rochester mean that there is currently no robust evidence that the zircon host rocks have avoided remagnetization since 3.0 Ga.

Unfortunately, the debate about the magnetism of Jack Hills zircons has become mired in minutiae in a way that most readers will find unilluminating. Additionally, a number of the statements by the Rochester group (Dare et al. 2016; Bono et al. 2016; 2018) are unsubstantiated [e.g., that there are "gross...errors in orientation and measurement" of Weiss et al. (2015)'s samples, that there is an "error in field sampling and/or reporting" by Weiss et al. (2015), and that the 12-mm diameter samples of Weiss et al. (2015) are of "insufficient volume…to accurately record…magnetization"; compare with Böhnel et al. (2009), Berndt et al. (2016), and Lima and Weiss (2016)]. Others of their statements are demonstrably false [e.g., that Weiss et al. (2015) "used an Ar atmosphere (B. Weiss, personal communication, 2014)" to thermally demagnetize their samples (they used an air atmosphere and never communicated otherwise to anyone), that Weiss et al. (2015) called for the existence of a "1 Ga overprint…that is seen everywhere" (they never claimed the cobbles have this overprint), and that somehow the fact that the MIT magnetometer is "located high in a tall, narrow building" is relevant for its sensitivity].

As a further example, Dare et al. (2016) and Bono et al. (2018) proposed that the 2G 755 magnetometer at U. Rochester is ~2 orders of magnitude more sensitive than the MIT 2G 755 magnetometer used for the Weiss et al. (2015) study. However, Wang et al. (2017) Fig. S5 showed that of 300 repeat measurements with the MIT magnetometer with no sample in the sense bore, 95% have moments below 9.9×10^{-13} Am^2. This means that the Rochester magnetometer, with a reported sensitivity of $\sim9\times10^{-13}$ Am^2, is at best trivially more sensitive than the MIT magnetometer.

Rather than further prolonging this unfruitful debate, a much more definitive approach would be for the MIT and Rochester laboratories to exchange samples, as we have repeatedly proposed over the last ~4 years (Weiss, 2017; Weiss et al., 2016). Sample exchange would be a straightforward way to test whether differences in the two laboratories' results stem from differences in measurement techniques or in sample magnetizations. We also invite independent, third-party laboratories to make their own measurements, for which we are happy to provide samples. Reproducibility tests like these form the foundation of the scientific method.

Appendix DR2. Measurement Methodology

1. Extraction and preparation of 11 zircon sets. We prepared 11 sets of zircons for magnetic field and compositional measurements (Table DR1). Zircon sets 1 and 2 were extracted from the rocks using a Frantz Model LB-1 Magnetic Separator (during which the grains were exposed to fields up to 1.6 T), washed in alcohol and then dated with U-Pb chronometry following Holden et al. (2009). Sets 3–9 were extracted nonmagnetically using heavy liquids at MIT. Following extraction, some zircons were cleaned with only alcohol while others were treated with HCl in an ultrasonicator with varying concentrations and for varying durations. Prior to magnetic analyses, all but sets 4, 9, and 11 were mounted in nonmagnetic epoxy and polished with alumina to approximately their mid-sections, while sets 4 and 9 were mounted in blind holes in a nonmagnetic glass slide following Fu et al. (2017). Set 10 was U-Pb dated and analyzed using electron microscopy by Bell et al. (2015). Set 11 was analyzed in situ in a 30 μm thin section of the host pebble conglomerate.

2. Quantum diamond microscopy (QDM) Measurements. For the QDM measurements, we used the instrument in vector magnetic microscopy (VMM) mode (Glenn et al., 2017). To extract the vector magnetic fields, we applied a 0.28 mT bias field normal to the diamond chip and 0.44 mT and 1.26 mT fields along the orthogonal transverse directions. We applied these fields in opposite directions in two independent measurements, which we later combined to separate the ferromagnetic and paramagnetic contributions from the zircons. In case of any slight difference between the positive and negative applied fields (which was at most ~0.01 mT), which can result in a uniform offset in the ferromagnetic images, we removed this offset to yield an offset-free ferromagnetic field map.

The noise floor in QDM measurements varies with experimental conditions, including the laser intensity, laser stability, laser polarization, applied microwave field, bias field strength, thermal stability, experiment duration, and diamond chip characteristics (Glenn et al., 2017). For these reasons, some of the QDM maps, particularly those of IRM (e.g., Fig. DR1), have a better noise floor and signal-to-noise ratio than others (e.g., NRM maps in Fig. DR4), Although we aim to maintain optimized sensitivity throughout QDM operation, the magnetic noise floor can vary depending on the above conditions and also on the differing challenges set by each rock sample.

Given the ~500 nT noise floor of the QDM in its high-resolution mode and our measurement height of <10 μm above the polished surface of the zircon, in the best-case scenario (where the magnetic source lies at the polished surface of the zircon), the minimum detectable moment of the zircons 3×10^{-15} Am^2. For an intermediate scenario where the source is buried 30 μm beneath the polished surface, the threshold was 2×10^{-13} Am^2. A zircon with a moment 1×10^{-12} Am^2 moment would be detectable even if the source is 60 μm inside the zircon; because most zircons have diameters of ~100-150 μm, an equivalent dipole at their centers would be detectable.

3. Possibility of contamination. Referring to our initial QDM study of Jack Hills zircons (Glenn et al., 2017), Bono et al. (2018) suggested that the preferential location of magnetization at the edges of our set 1 zircons may be due to contamination within our epoxy mounts or from polishing these mounts. The most compelling reason such contamination is unlikely for the vast majority of our set 1 zircons is that magnetic Fe-rich rinds were not observed around Bishop Tuff zircons (Fu et al., 2017) prepared and analyzed using techniques similar to those here. Here we provide additional analyses that support this conclusion.

With respect to contamination from polishing, our high resolution backscattered electron microscopy (BSEM) and wavelength dispersive spectroscopy (WDS) maps of selected zircon rims show that the secondary Fe-rich materials do not have a composition or texture resembling that of our polishing grits, which were alumina and diamond with grain sizes of 0.1-1 μm (Figs. DR2, 6).

To assess the frequency of contaminants in the epoxy, we consider the 78 zircons from set 1 (i.e., non-acid-washed) imaged in the high-resolution QDM mode (Fig. DR4C-D, G-L). The total area imaged by these maps is 9.87 mm^2 above the epoxy only and 1.95 mm^2 above zircons. The mean area per zircon is 0.024 mm^2 with a standard deviation of 0.006 mm^2. The total number of unambiguous contamination dipoles associated with the epoxy is 11. Assuming a Poisson process for magnetic contaminants falling on the sample with rate k = 1.11 mm^{-2}, then a typical zircon (area A = 0.024 mm^2) has a probability $P = 1 - \exp(kA) = 0.026$ to have one or more contamination dipoles land on top of it. The expected number of contamination dipoles over all zircons is N_{tot} = 1.11 $mm^{-2} \times 1.95\ mm^2 = 2.2$. Given that there are hundreds of dipoles over the 78 zircons, contamination associated with the epoxy mount is extremely unlikely to explain the magnetization at the edges of most zircons.

Appendix DR3. Comparison with Inclusion Study of Bell et al. (2015)

We briefly discuss our results in light of the Jack Hills zircon inclusion study by Bell et al. (2015). Drawing on their dataset, we find that of the 68 zircons they found to contain Fe oxides, just 6 (9%) contain Fe oxides not obviously associated with cracks or healed cracks, with the remainder clearly associated with these secondary textures (Fig. DR13). Raman spectroscopy showed that an Fe oxide inclusion in the crack of a Hadean grain (RSES77–5-7) is hematite. On the other hand, 5 of the 6 zircons found to have interior Fe oxides isolated from cracks and voids (making up 7% of the population), our energy dispersive spectroscopy (EDS) and cathodoluminescence (CL) analyses did not identify any Fe oxides in cracks or voids, meaning that there is a small population of Jack Hills zircons that may be candidates for containing ferromagnetic minerals that are dominantly primary. However, these grains may contain Fe oxides hidden in cracks and that are not exposed at the polished surface.

Figure DR1. Maps of the magnetization, texture and composition of Jack Hills zircons from set 1 (i.e., not acid-washed) other than those shown in Fig. 1. Shown are quantum diamond microscopy (QDM) maps of the out-of-the-plane component of the isothermal remanent magnetization (IRM) magnetic field superimposed on backscattered electron microscopy (BSEM) images (left), BSEM images (middle), and maps of Fe abundance from wavelength dispersive spectroscopy (right). Zircon in (A)-(J) have interior magnetic sources only, those in (K)-(L) did not have any detectable magnetic sources, and those in (N-O) have interior magnetic sources. (A) RSES199-1-17: Pb-Pb age of <3900 Ma. (B) RSES199-2-14 (Pb-Pb age of <3900 Ma). (C) RSES 199-2-17 (Pb-Pb age of <3900 Ma). (D) RSES 199-3-15 (Pb-Pb age <3900 Ma). Higher resolution BSEM and WDS data for boxed region are show in Fig. DR2. (E) RSES 199-3-17 (Pb-Pb age 3954 ± 9 Ma). (F) RSES 199-10-3 (Pb-Pb age <3900 Ma). (G) RSES 199-13-2 (Pb-Pb age 4189 ± 20 Ma). (H) RSES 199-14-3 (Pb-Pb age 4100 ± 10 Ma). (I) RSES 199-2-15 (Pb-Pb age <3900 Ma). (J) RSES 199-2-16 (Pb-Pb age 4053 ± 6 Ma). (K) RSES 199-9-9 (Pb-Pb age <3900 Ma). (L) RSES 199-10-1 (Pb-Pb age <3900 Ma). (M) RSES 199-1-14 (Pb-Pb age <3900 Ma). (O) RSES 199-12-2 (Pb-Pb age <3900 Ma). (P) RSES 199-4-17 (Pb-Pb age <3900 Ma). See Fig. DR3 for QDM data on all set 1 zircons. See Table DR4 for the Pb-Pb ages of these zircons.

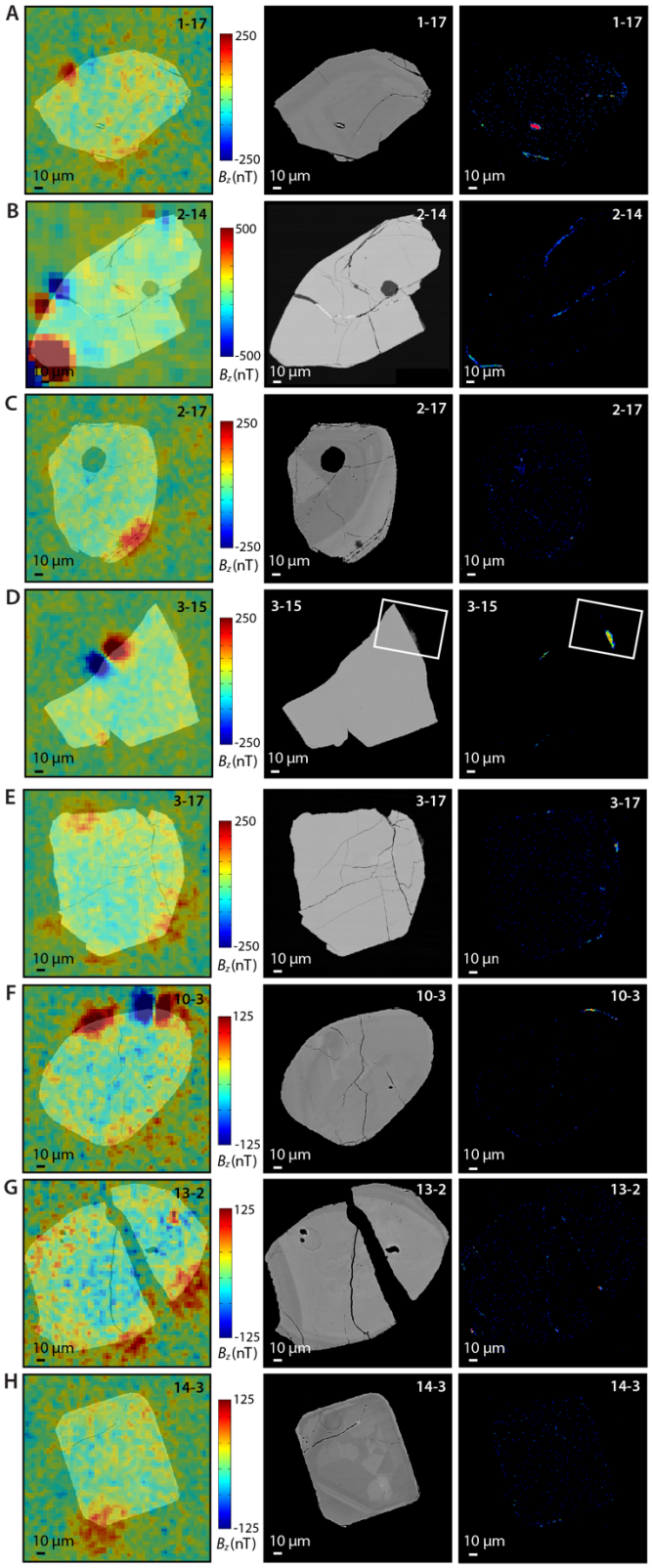
A
1-17
250
-250
B_z(nT)
10 µm
B
2-14
500
-500
C
2-17
D
3-15
E
3-17
F
10-3
125
-125
G
13-2
H
14-3

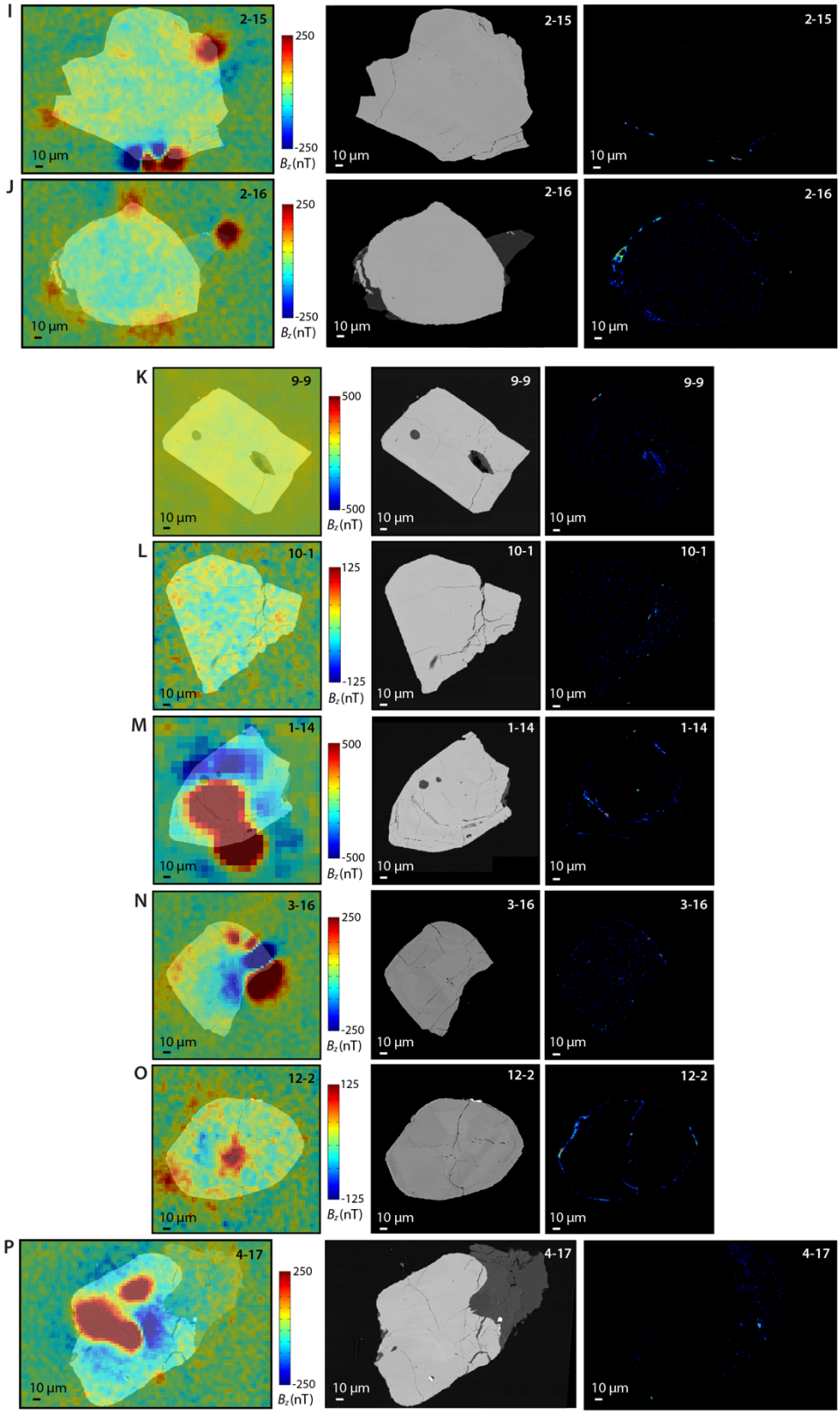
I
2-15
250
-250
B_z(nT)
10 µm
J
2-16
K
9-9
500
-500
L
10-1
125
-125
M
1-14
N
3-16
O
12-2
P
4-17

Fig DR2. High-resolution and multi-element electron microscopy analyses of Fe-rich rim on set 1 (i.e., non-acid washed) Jack Hills zircon RSES199-3-15 (see Fig. DR1D). (A) Backscattered electron microscopy (BSEM) image. White polygon shows location of measurements shown in (B-G). (B) BSEM image of polygon-shaped region. (C-G) Wavelength dispersive spectroscopy maps of Zr (C), F (D), Al (E), Si (F), and K (G). Note that he composition and texture of this rind are inconsistent with that of the 1 μm diamond grit used to polish our samples [e.g., Bono et al. (2018)].

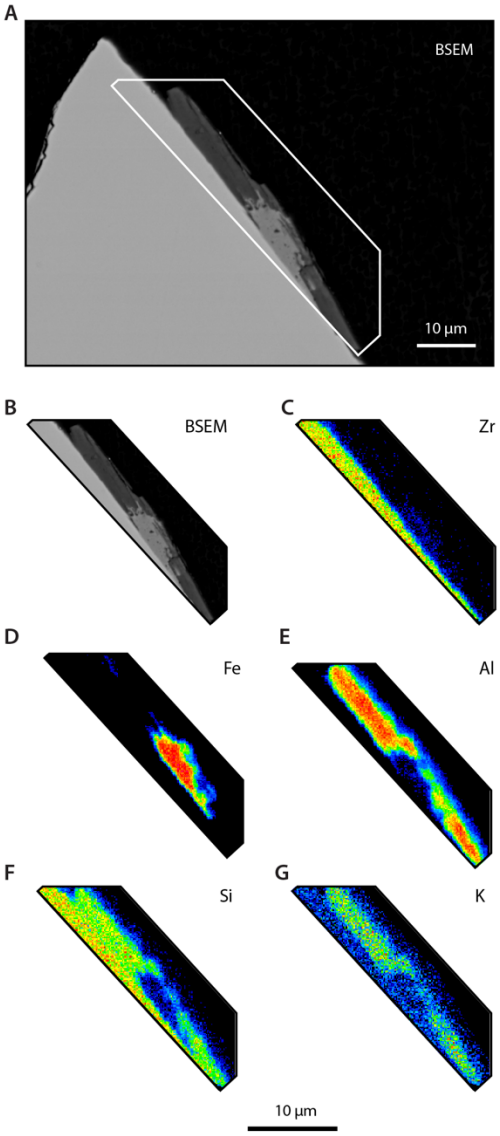
A
BSEM
10 µm
B
BSEM
C
Zr
D
Fe
E
Al
F
Si
G
K
10 µm

Figure DR3. QDM imaging of the IRM magnetic fields of all Jack Hills zircons analyzed from set 1. (A) Reflected light image of a matrix of zircons from the Jack Hills of Western Australia, polished and embedded in epoxy. Black boxes show fields-of-view imaged with QDM in (B-L). (B-L) Out-of-the-plane component of the magnetic field superimposed on reflected light image for corresponding fields-of-view in (A). Maps in (B, E, F, M) were acquired in the low-resolution mode, while the remaining maps were acquired with the high-resolution mode (see Appendix DR2). QDM maps were acquired at a height of 1-10 μm above the disk. As shown in four corners of each panel, zircons are identified with a two-digit code with their row number followed by their column number, with the zircon in row 1 and column 1 located at the uppermost left position on the epoxy mount and the zircon in row 1 and column 20 located at uppermost right position on the mount. Additional electron microscopy and X-ray tomography data were acquired for the following zircons: (B) Zircon 1-14 (see Fig. DR1M) and zircon 2-14 (see Fig. DR1B). (C) Zircon 1-15 (see Fig. 2), zircon 1-16 (see Fig. DR1E), zircon 1-17 (see Fig. DR1A), zircon 2-15 (see Fig. DR1I), zircon 2-16 (see Fig. DR1J), zircon 2-17 (see Fig. DR1C), zircon 3-15 (see Figs. DR1D and DR2), zircon 3-16 (see Fig. DR1N), zircon 3-17 (see Fig. DR1E), zircon 4-15 (see Fig. 1A), zircon 4-16 (see Fig. 1B), and zircon 4-17 (see Fig. DR1P). (G) Zircon 10-1 (see Fig. DR1L), zircon 10-2 (see Fig. 1B), zircon 10-3 (see Fig. DR1F), and zircon 12-2 (see Fig. DR1O). (J) Zircon 9-9 (see Fig. DR1K). (L) Zircon 13-2 (see Fig. DR1G), zircon 13-3 (see Fig. 1D), and zircon 14-3 (see Fig. DR1H). Circled zircons have Pb-Pb ages >3.9 Ga and uncircled ages have younger Pb-Pb ages. See Table DR4 for the Pb-Pb data for these zircons. Scale bars for are 300 μm.

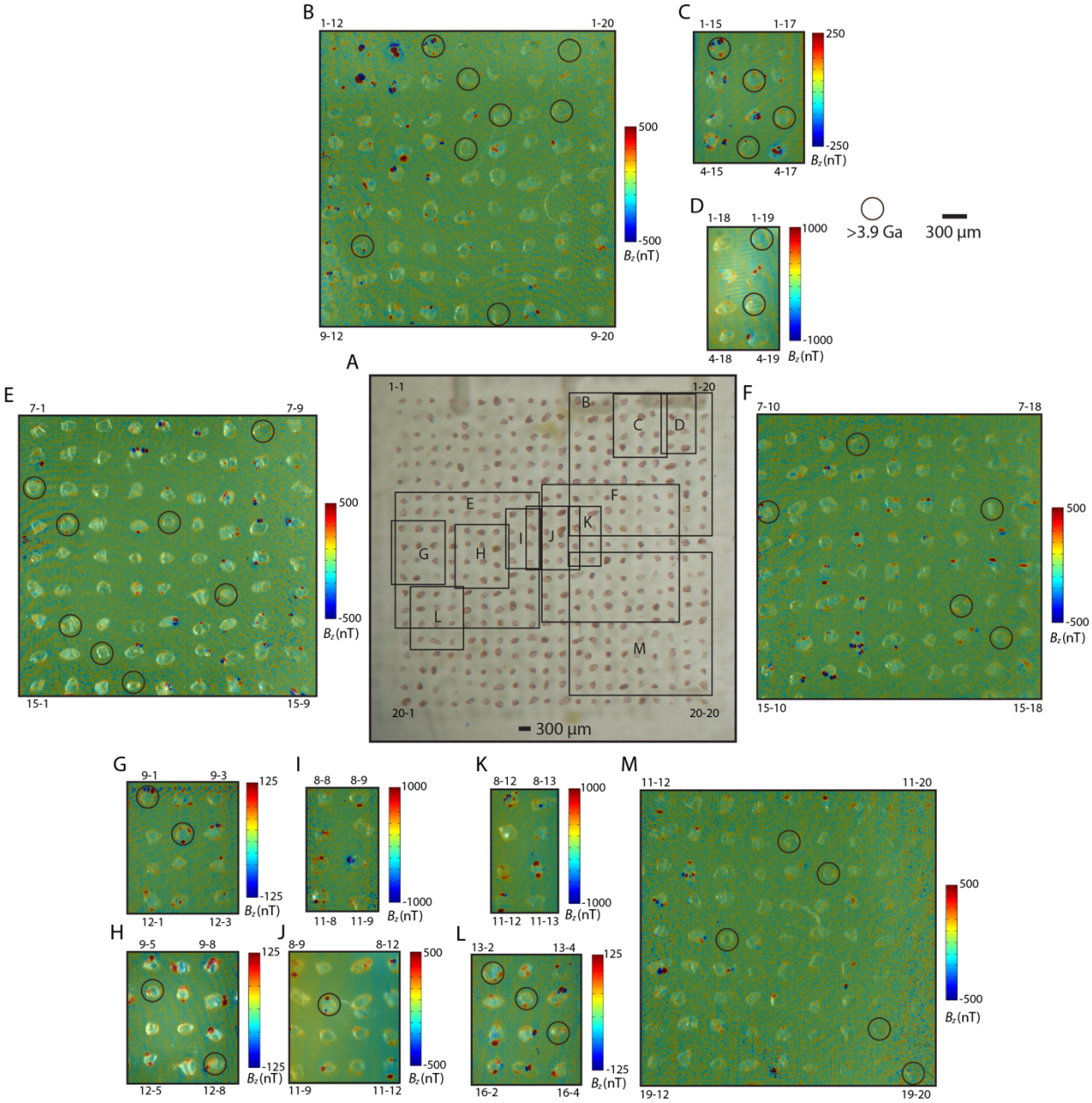
A
B
1-12
1-20
9-12
9-20
500
-500
B_z(nT)
C
1-15
1-17
4-15
4-17
250
-250
B_z(nT)
D
1-18
1-19
4-18
4-19
1000
-1000
B_z(nT)
>3.9 Ga
300 µm
E
7-1
7-9
15-1
15-9
500
-500
B_z(nT)
F
7-10
7-18
15-10
15-18
500
-500
B_z(nT)
1-1
1-20
20-1
20-20
300 µm
G
9-1
9-3
12-1
12-3
125
-125
B_z(nT)
H
9-5
9-8
12-5
12-8
125
-125
B_z(nT)
I
8-8
8-9
11-8
11-9
1000
-1000
B_z(nT)
J
8-9
8-12
11-9
11-12
500
-500
B_z(nT)
K
8-12
8-13
11-12
11-13
1000
-1000
B_z(nT)
L
13-2
13-4
16-2
16-4
125
-125
B_z(nT)
M
11-12
11-20
19-12
19-20
500
-500
B_z(nT)

Figure DR4. QDM imaging of the magnetic fields of Jack Hills zircons carrying natural remanent magnetization (NRM) in sets 3 (i.e., not acid-washed) and sets 5 and 6 (i.e., washed in 0.5 N HCl for 2 and 20 h, respectively). Shown are maps out-of-the-plane component of the magnetic field superimposed on transmitted light images of each zircon. QDM maps were acquired at a height of 1-10 μm above the disk. Zircons in (A-D) are from set 3, those in (E-G) are from set 5 and those in (H-J) are from set 6. See Figs. DR5-6 for compositional maps of some of the set 6 zircons shown here. Scale bar is 100 μm. (A) Zircons D175M-A1-1-1 (top) and D175M-A1-2-1 (bottom). (B) Zircons D175M-A1-1-1 (top left), D175M-A1-2-1 (bottom left), D175M-A1-1-2 (top right), and D175M-A1-2-2 (bottom right). (C) Zircons D175M-A1-5-2 (top) and D175M-A1-6-2 (bottom). (D) Zircons D175M-A1-4-3 (top) and D175M-A1-5-3 (bottom). (E) Zircons D175M-A2-4-4 (top) and D175M-A2-5-4 (bottom). (F) Zircons D175M-A2-6-4 (top) and D175M-A2-7-4 (bottom). (G) Zircons D175M-A2-4-5 (top) and D175M-A2-5-5 (bottom). (H) Zircons D175M-A3-4-6 (top) and D175M-A3-5-6 (bottom). (I) Zircons D175M-A3-5-7 (top) and D175M-A3-6-7 (bottom). (J) Zircons D175M-A3-5-8 (top) and D175M-A3-6-8 (bottom).

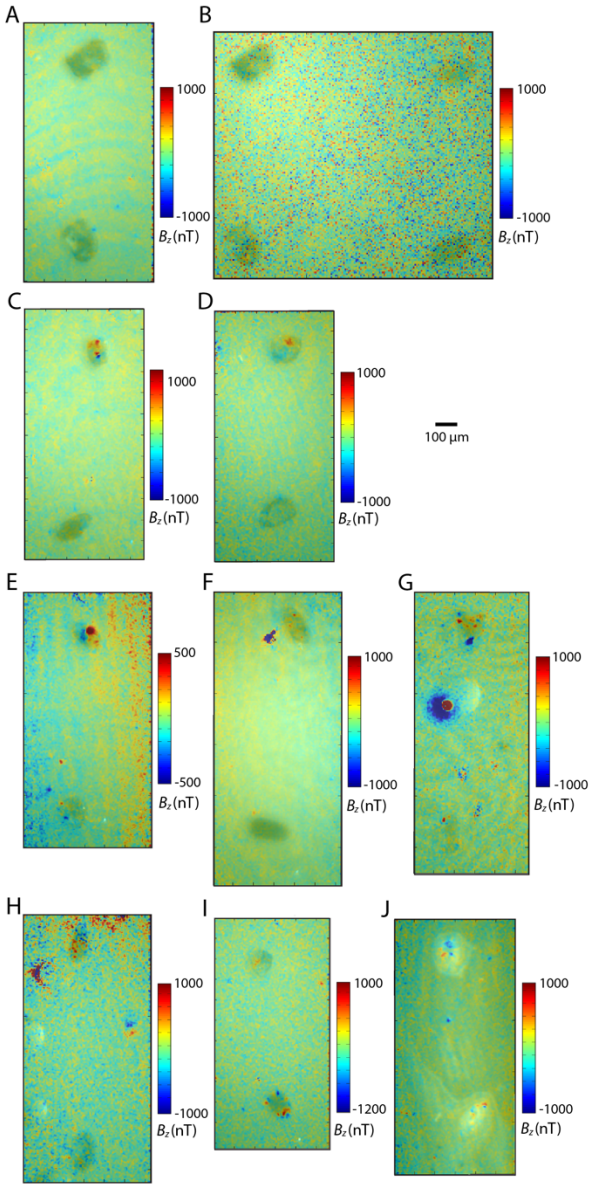
A
1000
-1000
B_z(nT)
B
1000
-1000
B_z(nT)
C
1000
-1000
B_z(nT)
D
1000
-1000
B_z(nT)
100 μm
E
500
-500
B_z(nT)
F
1000
-1000
B_z(nT)
G
1000
-1000
B_z(nT)
H
1000
-1000
B_z(nT)
I
1000
-1200
B_z(nT)
J
1000
-1000
B_z(nT)

Figure DR5. SEM maps of the magnetization, texture and composition of Jack Hills zircons from set 6 (i.e., treated with 0.5 N HCl for 20 h). (A) Zircon D175M-A3-6-7. (B) Zircon D175M-A3-6-8. See Fig. DR4 for QDM maps of zircons analyzes from sets 3, 5, and 6. Higher resolution BSEM and WDS data for boxed region are show in Fig. DR6.

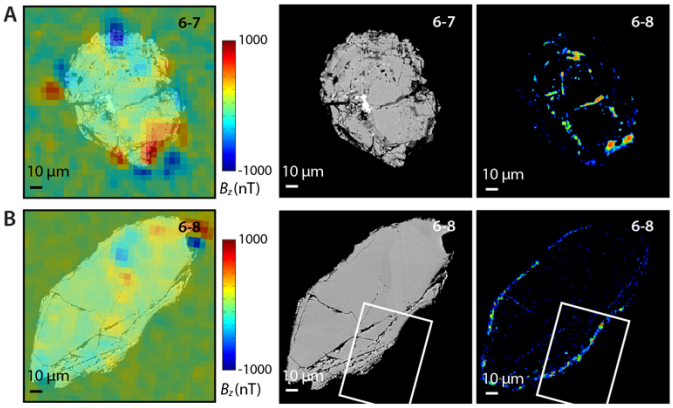
A
6-7
1000
-1000
B_z(nT)
10 µm
6-7
10 µm
6-8
10 µm
B
6-8
1000
-1000
B_z(nT)
10 µm
6-8
10 µm
6-8
10 µm

Figure DR6. High-resolution and multi-element electron microscopy analyses of Fe-rich rim on set 6 (i.e., treated with 0.5 N HCl for 20 h) Jack Hills zircon D175M-A3-6-8 (see Fig. DR5B). (A) Backscattered electron microscopy (BSEM) image. White polygon shows location of measurements shown in (B-G). (B) BSEM image of polygon-shaped region in (A). (C-G) Wavelength dispersive spectroscopy maps of Zr (C), F (D), Al (E), Si (F), and O (G). Note that he composition and texture of this rind is inconsistent with that of the 0.1-1 μm alumina (Al_2O_3) grit used to polish our samples [e.g., Bono et al. (2018)].

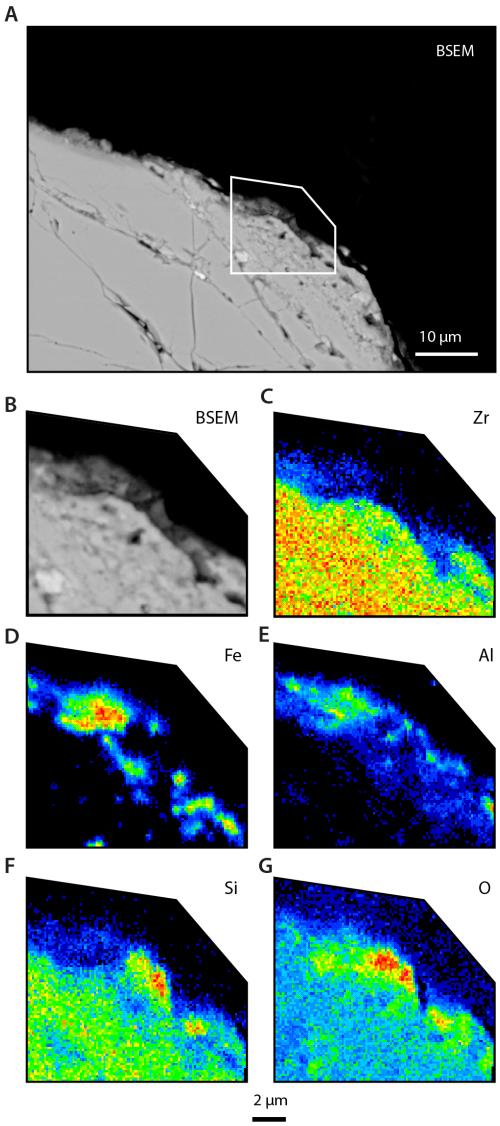
A
BSEM
10 µm
B
BSEM
C
Zr
D
Fe
E
Al
F
Si
G
O
2 µm

Figure DR7. Analysis of detrital zircons in situ in a 30 μm thin section of the Erawandoo Hill quartz pebble conglomerate. Although some zircons have weak magnetic anomalies, most of the magnetization is associated with the boundaries between quartz grains. (A, B) QDM maps of the out-of-the-plane component of the IRM magnetic field superimposed on transmitted light crossed polar photomicrographs. Most grains are quartz, but grain boundaries commonly have secondary minerals including clays and Fe oxides. Zircons are identified with arrows. The heights of panels (A) and (B) are each ~700 μm, meaning they are each similar in size to the single microconglomerate test samples in the study of Tarduno et al. (2015). (C, D) BSEM images of the boxed regions in (A) and (B), respectively. The magnetic anomalies in (A, B) are shown to commonly correspond with cracks and alteration textures.

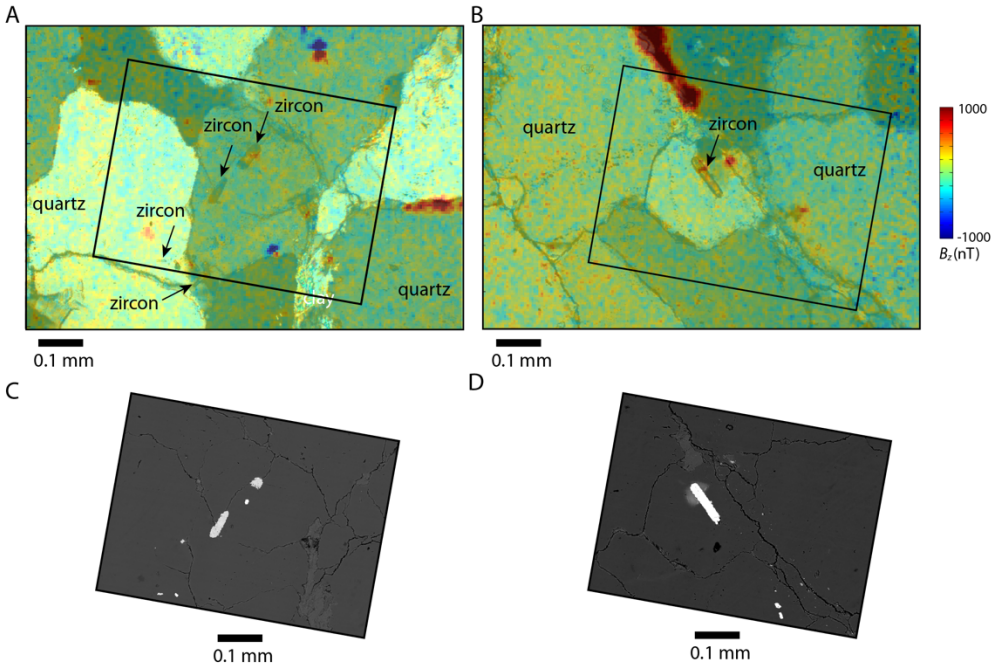
A
B
zircon
zircon
zircon
zircon
quartz
quartz
quartz
quartz
1000
-1000
B_z (nT)
0.1 mm
0.1 mm
C
D
0.1 mm
0.1 mm

Figure DR8. (A) Raman spectrum of zircon RSES 57-2-13 (Pb-Pb age 4016 ± 6 Ma). The zircon exhibits peaks at wavenumbers corresponding to those of zircon (Nasdala et al., 1995) (blue) and hematite (red) standards (de Faria and Lopes, 2007). (B) Transmitted light photomicrograph of zircon showing location where Raman spectrum was acquired (white circle). The image is approximately 0.3 mm across.

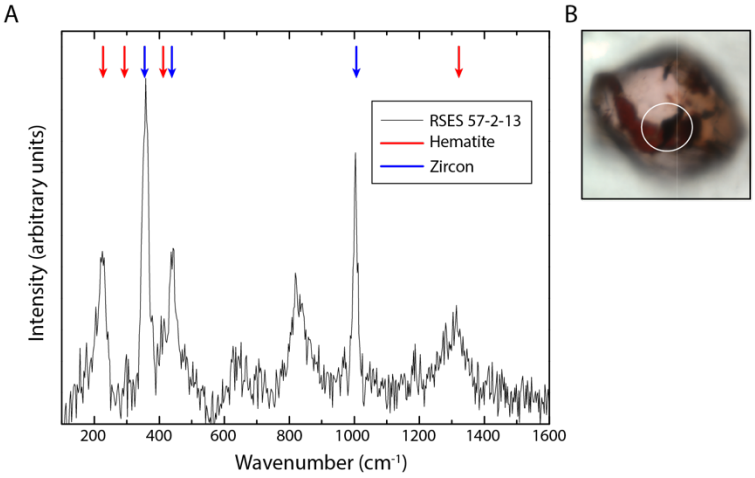
A
B
RSES 57-2-13
Hematite
Zircon
Intensity (arbitrary units)
Wavenumber (cm-1)
200
400
600
800
1000
1200
1400
1600

Figure DR9. Thermal demagnetization data for non-acid-washed Jack Hills zircons carrying IRM (i.e., set 2) not shown in Fig. 3. Shown is the magnetic moment inferred from SQUID microscopy (SM) maps following each thermal demagnetization step (0°C denotes no heating). Red points indicate a second thermal demagnetization of IRM experiment conducted after the zircons had been heated to 680°C. Blue points equal the IRM intensity after two repeat thermal demagnetization experiments to 680°C. Zircons in (A-F) are inferred to all contain hematite (Curie temperature 675°C) with some also containing goethite (Curie temperature 50-120°C). Zircon in (G) is inferred to contain both hematite and magnetite (Curie temperature 580°C), while zircon in (H) has uncertain magnetic mineralogy. All zircons except those in (D) and (H) were found to contain origin-trending, single-component IRMs; the two-component magnetization in zircon in (D) likely results from the fact that our 400 mT IRM did not completely overprint the <1.6 T IRM from the Frantz. Dashed lines indicate demagnetization steps in which the magnetic moment no longer exhibits directional coherence in orthographic projection plots. (A) Zircon RSES 57-9-19 (Pb-Pb age <3900 Ma). (B) Zircon RSES 57-1-3 (Pb-Pb age 4039 ± 7 Ma). (C) Zircon RSES 57-4-15 (Pb-Pb age <3900 Ma). (D) Zircon RSES 57-3-19 (Pb-Pb age <3900 Ma). (E) Zircon RSES 57-19-20 (Pb-Pb age <3900 Ma). Note that this zircon's magnetization direction remains within 50° of the original undemagnetized IRM direction until the final demagnetization step of 674°C. (F) Zircon RSES 57-15-11 (Pb-Pb age 4048 ± 9 Ma). (G) Fragment A of zircon RSES 57-6-19 (Pb-Pb age <3900 Ma). Thermal demagnetization of another fragment of this zircon is shown in Fig. 3A. (H) Zircon RSES 57-19-12 (Pb-Pb age 4124 ± 6 Ma). See Table DR4 for the Pb-Pb data for these zircons.

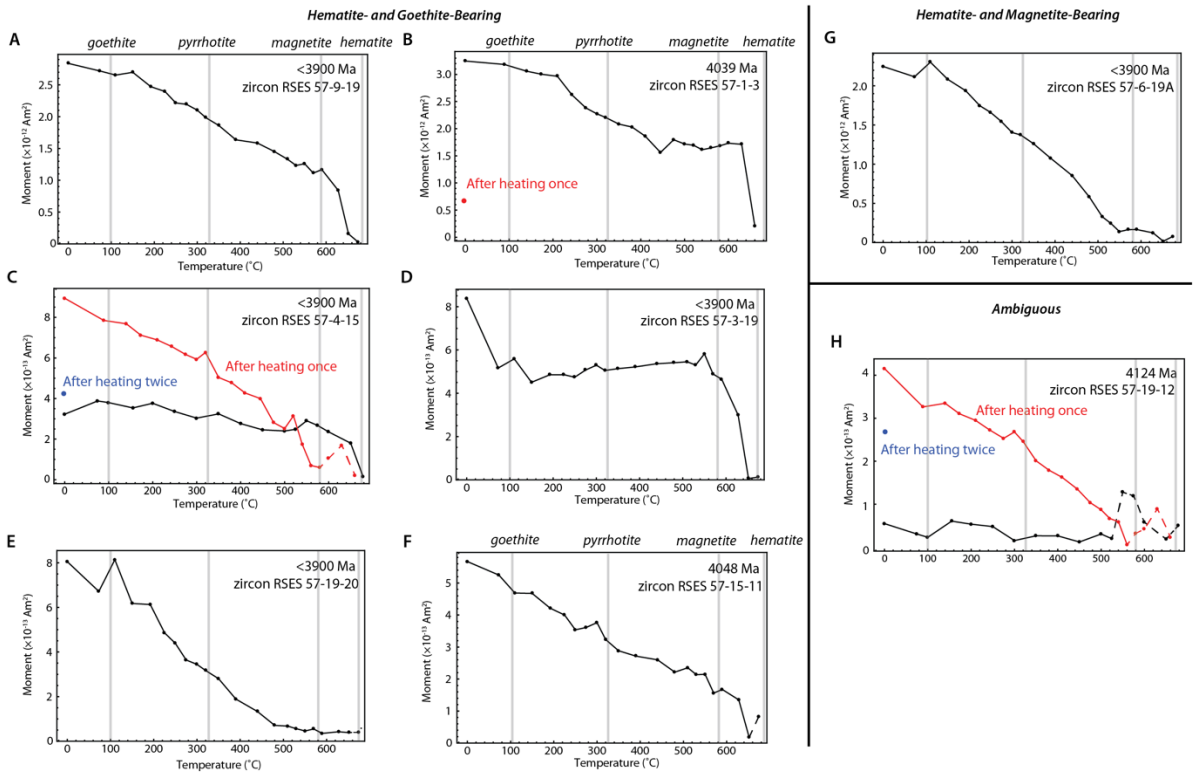
Hematite- and Goethite-Bearing
A
goethite
pyrrhotite
magnetite
hematite
<3900 Ma
zircon RSES 57-9-19
Moment (×10^-12 Am²)
Temperature (°C)
B
4039 Ma
zircon RSES 57-1-3
After heating once
C
<3900 Ma
zircon RSES 57-4-15
After heating once
After heating twice
D
<3900 Ma
zircon RSES 57-3-19
E
<3900 Ma
zircon RSES 57-19-20
F
4048 Ma
zircon RSES 57-15-11
Hematite- and Magnetite-Bearing
G
<3900 Ma
zircon RSES 57-6-19A
Ambiguous
H
4124 Ma
zircon RSES 57-19-12
After heating once
After heating twice

Figure DR10. SM maps of the NRM of zircons from sets 4 (i.e., non-acid-washed) and set 9 (washed with 6 N HCl for 12 minutes) mounted in two polished epoxy disks. Shown is the vertical component of the magnetic at a height of 170 μm above the disk. (A) Set 4. (B) Set 9.

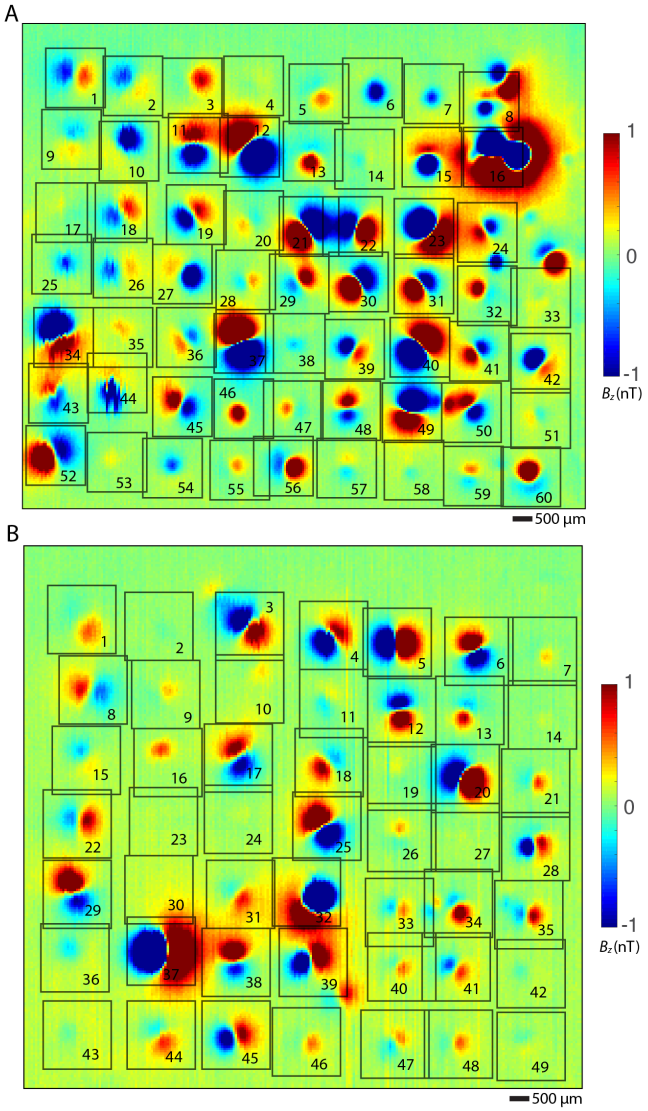
A
1
0
-1
B_z(nT)
500 µm
B
1
0
-1
B_z(nT)
500 µm

Figure DR11. Maps of magnetization, texture and composition of Jack Hills zircons washed with 6 N HCl for 12 minutes (i.e., set 7) and 1 h (i.e., set 8) not shown in Fig. 4. Shown are QDM maps of the out-of-the-plane component of the IRM magnetic field superimposed on BSEM images (left), BSEM images (middle), and maps of Fe abundance from wavelength dispersive spectroscopy (right). (A) Zircon D175M-B1-4-2. (B) Zircon D175M-B1-4-1. (C) Zircon D175M-B1-3-2. (D) Zircon D175M-B2-1-4. (E) Zircon D175M-B2-2-5. (F) Zircon D175M-B2-3-5. (G) Zircon D175M-B1-3-1. (H) Zircon D175M-B2-1-5.

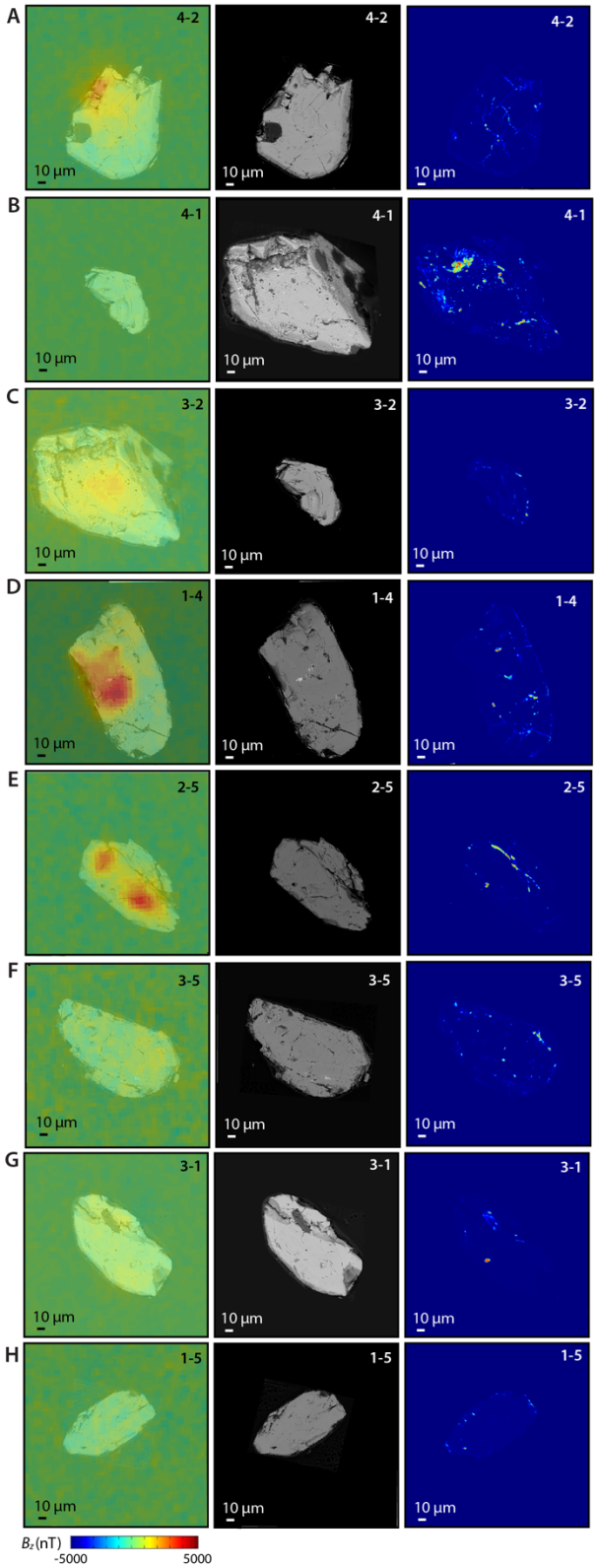
A
4-2
10 µm
B
4-1
C
3-2
D
1-4
E
2-5
F
3-5
G
3-1
H
1-5
B_z (nT)
-5000
5000

Figure DR12. QDM imaging of the IRM magnetic fields of all Jack Hills zircons from sets 7 (i.e., washed in 6 N HCl for 12 min) and 8 (i.e., washed in 6 N HCl for 1 h). Shown are maps out-of-the-plane component of the magnetic field superimposed on transmitted light images of each zircon. QDM maps were acquired at a height of 1-10 µm above the disk. Zircons in (A-B), (F-H), and (J-L) are from set 7 and those in (C-E), (I), and (M-N) are from set 8. See Figs. 4 and DR11 for compositional maps of some of the zircons shown here. Scale bar is 100 µm. Sets 7 and 8 were mounted on one epoxy disk; the maps are arranged such that the zircons are in the same approximate locations that they have on the epoxy disk. (A) Zircons D175M-B1-1-1 (top) and D175M-B1-2-1 (bottom). (A) Zircons D175M-B1-1-2 (top) and D175M-B1-2-2 (bottom). (C) Zircons D175M-B1-1-4 (top) and D175M-B2-2-4 (bottom). (D) Zircons D175M-B2-1-5 (top) and D175M-B2-2-5 (bottom). (E) Zircons D175M-B2-1-6 (top) and D175M-B2-2-6 (bottom). (F) Zircons D175M-B1-3-1 (top) and D175M-B1-4-1 (bottom). (G) Zircons D175M-B1-3-2 (top) and D175M-B1-4-2 (bottom). (H) Zircons D175M-B1-3-3 (top) and D175M-B1-4-3 (bottom). (I) Zircons D175M-B2-3-5 (top) and D175M-B2-4-5 (bottom). (J) Zircons D175M-B1-4-1 (top) and D175M-B1-5-1 (bottom). (K) Zircons D175M-B1-4-2 (top) and D175M-B1-5-2 (bottom). (L) Zircons D175M-B1-4-3 (top) and D175M-B1-5-3 (bottom). (M) Zircons D175M-B2-4-4 (top) and D175M-B2-5-4 (bottom). (M) Zircons D175M-B2-4-5 (top) and D175M-B2-5-5 (bottom).

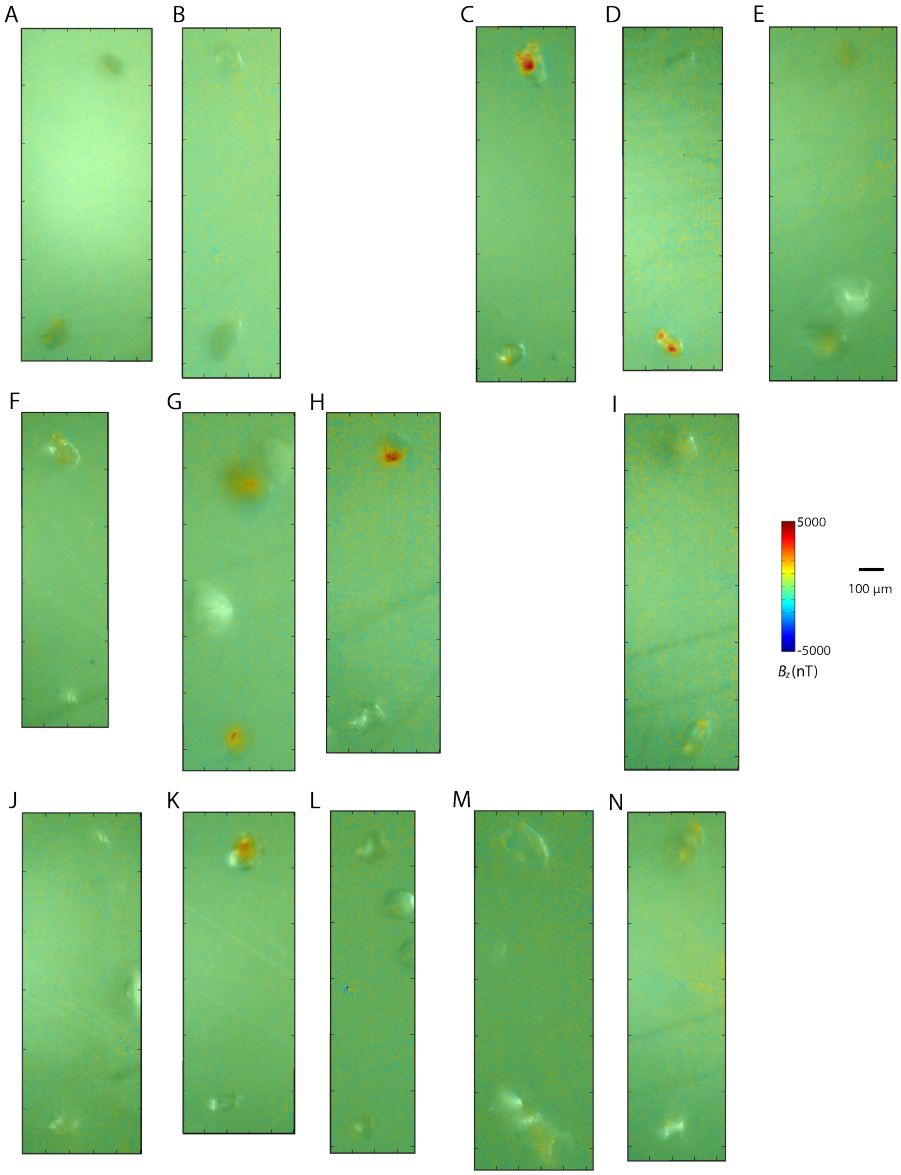
A
B
C
D
E
F
G
H
I
J
K
L
M
N
5000
-5000
B_z(nT)
100 μm

Figure DR13. The association of secondary textures and Fe oxides in Jack Hills zircons. Shown are examples of zircons intersected by cracks [(A), top iron oxide in (B) and large Fe oxide at bottom left of (F)], filling cracks [bottom Fe oxide in (B)], filling cracks (C), intersected by annealed cracks (D, E), and isolated from any visible cracks [upper right Fe oxide in (F)]. (A) BSEM image of zircon RSES 80-10-8 (Pb-Pb age 3360 ± 9 Ma). (B) BSEM image of zircon RSES 80-9-20 (Pb-Pb age 3389 ± 5 Ma). (C) BSEM image of zircon RSES 86-4-18 (Pb-Pb age 4078 ± 7 Ma). (D) BSEM image of zircon RSES 82-1-5 (Pb-Pb age 3408 ± 36 Ma). (E) Cathodoluminescence image of grain in (C) with annealed crack circled. (F) BSEM image of zircon RSES 82-14-13 (Pb-Pb age 3342 ± 4 Ma). (G) Cathodoluminescence image of grain in (F). See Table DR4 for the Pb-Pb data for these zircons. Data acquired as part of the inclusion study by Bell et al. (2015).

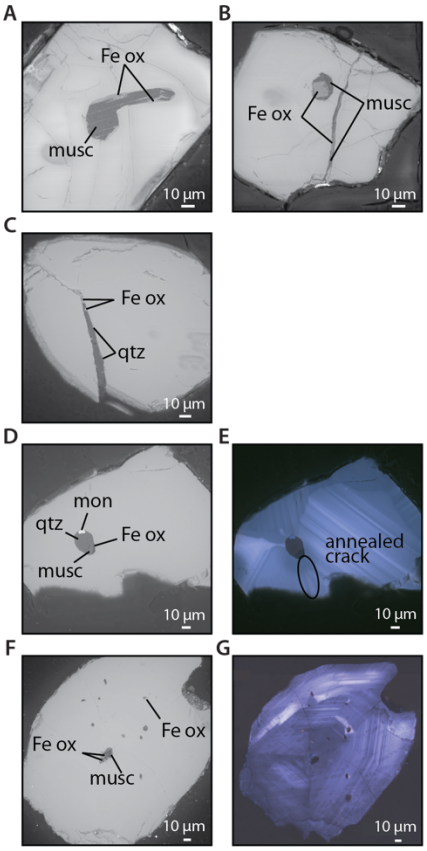
A
Fe ox
musc
10 µm
B
Fe ox
musc
10 µm
C
Fe ox
qtz
10 µm
D
mon
qtz
Fe ox
musc
10 µm
E
annealed
crack
10 µm
F
Fe ox
Fe ox
musc
10 µm
G
10 µm

Table DR1. Preparation and measurement details for the sets of zircons analyzed in this study.

Set	Cleaning	Source	Mount	U-Pb?	Magnetization	*N*	Instrument	Other Analyses
1	Alcohol	RSES 199	Epoxy	Yes	Frantz IRM	257	QDM[2]	BSEM[3], CL[3], WDS[3]
2	Alcohol	RSES 57	Glass	No	Frantz IRM + 400 mT IRM[1]	10	SM[3]	Raman[4]
3	Alcohol	D175M-A1	Epoxy	No	NRM	8	QDM[2]	-
4	Alcohol	D175H-A1	Glass	No	NRM	60	SM[3]	-
5	0.5 N HCl for 2 h	D175M-A2	Epoxy	No	NRM	6	QDM[2]	-
6	0.5 N HCl for 20 h	D175M-A3	Epoxy	No	NRM	6	QDM[2]	BSEM[3], WDS[3]
7	6 N HCl for 12 min	D175M-B1	Epoxy	No	vertical IRM 400 mT	13	QDM[2]	BSEM[5], CL[5], EDS[5], X-ray[6]
8	6 N HCl for 1 h	D175M-B2	Epoxy	No	vertical IRM 400 mT	11	QDM[2]	BSEM[5], CL[5], EDS[5], X-ray[6]
9	6 N HCl for 12 min	D175H-A2	Glass	No	NRM	49	SM[3]	
10	Alcohol	RSES 80, 82, and 86	Epoxy	Yes	-	0	-	BSEM[7], EDS[7], CL[7], Raman[4]
11	None	D175C	Thin Section	No	vertical IRM 400 mT	5	QDM[2]	TL[3], BSEM[3]

Notes: The first column gives name of each zircon set, the second column lists how the zircons were cleaned, the third column lists the name of the zircon parent blocks, the fourth column lists the nature of the zircon mount (polished epoxy or drilled glass disk), the fifth columns lists whether the zircons were dated with U-Pb chronometry, the sixth column lists the form of magnetization analyzed [NRM = natural remanent magnetization, Frantz IRM = randomly-oriented near-saturation (up to 1.6 T) isothermal remanent magnetization from Frantz magnetic separator at ANU (see main text), IRM = isothermal remanent magnetization in MIT Paleomagnetism Laboratory], the seventh column lists the number of zircons analyzed magnetically, the eighth column lists the magnetometer used for the analyses (QDM = quantum diamond microscopy, SM = SQUID microscope), and the ninth column lists other analyses (BSEM = backscattered electron microscopy, WDS = wavelength dispersive spectroscopy, EDS = energy dispersive spectroscopy, CL = cathodoluminescence, X-ray = X-ray tomography, Raman = Raman spectroscopy), TL = transmitted light optical microscopy. For the CL data, only those of Bell et al. (2015) are shown in this study.

[1]The 400 mT IRM field was applied on zircons previously exposed to the Frantz magnetic separator. All zircons in set 2 were given this 400 mT IRM except for zircons 57-4-15 and 57-19-12. The 400 mT IRM field was applied to each zircon prior to mounting them in the glass disk, such that the magnetization directions of the zircons are expected to be randomly oriented after final mounting for SM analyses. The moments of these samples were then repeatedly measured during progressive thermal demagnetization conducted in air to 680 °C in using an ASC Scientific TD-48SC oven.
[2]Conducted at Harvard University
[3]Conducted at the Massachusetts Institute of Technology
[4]Conducted at the Geophysical Laboratory, Carnegie Institution of Science prior to thermal demagnetization
[5]Conducted at the University of Cambridge
[6]Conducted at Carl Zeiss X-Ray Microscopy, Inc.
[7]Conducted at the University of California, Los Angeles as part of the study by Bell et al. (2015). A total of 2,450 zircons were analyzed.

Table DR2. Statistics on locations of magnetization sources in zircons imaged with QDM.

Set	Cleaning	Pixel size (μm)/mode	Analyzed	Detected	Exterior-Only Sources	Interior Sources
1	alcohol	8.7 (low res)	257	147	122	25
1	alcohol	3.6 (hi res)	78	71	52	19
3	alcohol	7.3 (low res)	4	0	-	-
3	alcohol	4.8 (hi res)	6	5	3	2
5	0.5 N HCl for 2 h	4.8 (hi res)	6	5	3	2
6	0.5 N HCl for 20 h	4.8 (hi res)	6	4	3	1
7	6 N HCl for 12 min	4.8 (hi res)	13	6	2	4
8	6 N HCl for 1 h	4.8 (hi res)	11	8	2	6

Note: The first column gives name of each zircon set, the second column lists how the zircons were cleaned, the third column lists the QDM pixel size for each set of images (and denoting whether mode was low or high resolution), the fourth column lists the number of zircons analyzed, the fifth columns lists the number of zircons whose magnetizations were detected, the sixth column lists the number of zircons with exterior-only magnetization sources

(defined to be within ~20 μm of the zircons' rims), and the seventh column lists the number of zircons with interior magnetization sources.

Table DR3. Statistics of NRM intensity measured using the SM for sets 4 (non-acid-washed) and 9 (washed with 6 N HCl)

Set	Statistic	Value
4	Number of Zircons Measured	60
	Number of Zircons Detected	60
	Minimum NRM (Am^2)	2.17×10^{-14}
	Maximum NRM (Am^2)	4.34×10^{-12}
	Mean NRM (Am^2)	8.26×10^{-13}
	Median NRM (Am^2)	4.57×10^{-13}
	% Zircons with NRM < 1×10^{-13} Am^2	13.3
	% Zircons with NRM > 1×10^{-12} Am^2	23.3
9	Number of Zircons Measured	49
	Number of Zircons Detected	47
	Minimum NRM (Am^2)	<~1.0×10^{-14}
	Maximum NRM (Am^2)	5.15×10^{-12}
	Mean NRM (Am^2)	4.88×10^{-13}
	Median NRM (Am^2)	1.98×10^{-13}
	% Zircons with NRM < 1×10^{-13} Am^2	32.7
	% Zircons with NRM > 1×10^{-12} Am^2	12.2

Note: The first column gives identity of each zircon set, the second column lists the statistic, and the third column gives the value of the statistic.

Table DR4. Pb-Pb ages of set 1, 2, and 10 zircons.

Set	Zircon Name	$^{207}Pb/^{206}Pb$ Age (Ma)	1σ Uncertainty (Ma)	% Discordant	Reference
1					Holden et al. (2009)
	RSES 199-1-4	4216	9.4	-2	
	RSES 199-1-15	4019	5.2	0	
	RSES 199-1-19	3977	4.9	5	
	RSES 199-2-16	4053	6.0	1	
	RSES 199-3-17	3954	9.0	147	
	RSES 199-3-19	4118	6.6	-2	
	RSES 199-4-16	3973	8.2	91	
	RSES 199-7-8	4101	10.7	-2	
	RSES 199-7-13	3975	5.0	-1	
	RSES 199-9-1	4056	5.8	-1	
	RSES 199-9-10	3982	5.6	95	
	RSES 199-9-17	3994	8.0	-1	
	RSES 199-10-2	4050	7.9	85	
	RSES 199-10-5	4036	13.5	3	
	RSES 199-12-7	4032	4.9	7	
	RSES 199-12-16	4100	6.6	0	
	RSES 199-13-2	4189	20.0	-3	
	RSES 199-13-17	4023	8.5	-3	
	RSES 199-14-3	4100	9.7	3	
	RSES 199-15-4	4117	5.6	-3	
	RSES 199-15-14	3970	9.2	23	
	RSES 199-18-19	4095	12.7	-3	
	RSES 199-19-20	4053	6.0	-4	
	RSES 199-20-3	4028	10.9	0	
	RSES 199-20-8	4083	5.3	5	
	All other RSES 199 zircons	<3900	-	-	
2					Holden et al. (2009)

RSES 57-1-3	4039	7.2	-1	
RSES 57-2-13	4016	5.5	-7	
RSES 57-3-19	<3900	-	-	
RSES 57-4-15	<3900	-	-	
RSES 57-6-19	<3900	-	-	
RSES 57-9-19	<3900	-	-	
RSES 57-15-11	4048	9.5	0	
RSES 57-19-12	4124	6.1	-5	
RSES 57-19-20	<3900	-	-	
				Bell et al. (2015)
RSES 80-9-20	3389	5	1	
RSES 80-10-8	3360	9	27	
RSES 82-1-5	3408	36	9	
RSES 82-14-13	3342	4	2	
RSES 86-4-18	4078	7	-5	

Note: The first column gives name of each zircon set, the second column gives identity of each zircon, the third column lists the $^{207}Pb/^{206}Pb$ age, the fourth column gives the 1-standard deviation uncertainty on the $^{207}Pb/^{206}Pb$ age, the fifth column gives the concordance, calculated as $100 \times (t_{207/206} - t_{206/238})/t_{206/238}$, where $t_{207/206}$ and $t_{206/238}$ are the $^{207}Pb/^{206}Pb$ and $^{206}Pb/^{238}U$ ages, respectively, and the final column gives the reference for the Pb-Pb ages for each set of zircons.

Movie DR1. Animation showing X-ray tomography of 4019 ± 5 Ma Jack Hills detrital zircon RSES 199-1-15 (not acid-washed). Grain is viewed from different orientations and with differing density thresholds so that the interior and exterior of the grain become visible. Data were acquired with the ZEISS Xradia 520 Versa. Red voxels have high X-ray absorption relative to that of zircon host (grey) and are inferred to be Fe-rich particles. The movie shows that these high-absorption materials are confined to the exterior of the grain.

Supplementary References

Bell, E. A., Boehnke, P., Hopkins-Wielicki, M. D., and Harrison, T. M., 2015, Distinguishing primary and secondary inclusion assemblages in Jack Hills zircons: Lithos, v. 234-235, p. 15-26.

Berndt, T., Muxworthy, A. R., and Fabian, K., 2016, Does size matter? Statistical limits of paleomagnetic field reconstruction from small rock specimens: J. Geophys. Res., v. 121, p. doi:10.1002/2015JB012441.

Böhnel, H., Michalk, D., Nowaczyk, N., and Gonzalez Naranjo, G., 2009, The use of mini-samples in palaeomagnetism: Geophys. J. Int., v. 179, p. 35-42.

Bono, R. K., Tarduno, J. A., Dare, M. S., Mitra, G., and Cottrell, R. D., 2018, Cluster analysis on a sphere: Application to magnetizations from metasediments of the Jack Hills, Western Australia: Earth Planet. Sci. Lett., v. 484, p. 67-80.

Dare, M. S., Tarduno, J. A., Bono, R. K., Cottrell, R. D., Beard, J. S., and Kodama, K. P., 2016, Detrital magnetite and chromite in Jack Hills quartzite cobbles: Further evidence for the preservation of primary magnetizations and new insights into sediment provenance: Earth Planet. Sci. Lett., v. 451, p. 298-314.

de Faria, D. L. A., and Lopes, F. N., 2007, Heated goethite and natural hematite: Can Raman spectroscopy be used to differentiate them?: Vib. Spectrosc., v. 45, p. 117-121.

Fu, R. R., Weiss, B. P., Lima, E. A., Kehayias, P., Araujo, J. F. D. F., Glenn, D. R., Gelb, J., Einsle, J. F., Bauer, A. M., Harrison, R. J., Ali, G. A. H., and Walsworth, R. L., 2017, Evaluating the paleomagnetic potential of single zircon crystals using the Bishop Tuff: Earth Planet. Sci. Lett., v. 458, p. 1-13.

Glenn, D. R., Fu, R. R., Kehayias, P., Le Sage, D., Lima, E. A., Weiss, B. P., and Walsworth, R. L., 2017, Micrometer-scale magnetic imaging of geological samples using a quantum diamond microscope: Geochem. Geophys. Geosyst., v. 18, p. doi:10.1002/2017GC006946.

Holden, P., Lanc, P., Ireland, T. R., Harrison, T. M., Foster, J. J., and Bruce, Z., 2009, Mass-spectrometric mining of Hadean zircons by automated SHRIMP multi-collector and single-collector U/Pb zircon age dating: The first 100,000 grains: Int. J. Mass Spectrom., v. 286, p. 53-63.

Lima, E. A., and Weiss, B. P., 2016, Ultra-high sensitivity moment magnetometry of geological samples using magnetic microscopy: Geochem. Geophys. Geosyst., v. 17, p. doi:10.1002/2016GC006487.

Nasdala, L., Irmer, G., and Wolf, D., 1995, The degree of metamictization in zircon: a Raman spectroscopic study: Eur. J. Mineral., v. 7, p. 471-478.

Tarduno, J. A., and Cottrell, R. D., 2013, Signals from the ancient geodynamo: A paleomagnetic field test on the Jack Hills metaconglomerate: Earth Planet. Sci. Lett., v. 367, p. 123-132.

Tarduno, J. A., Cottrell, R. D., Davis, W. J., Nimmo, F., and Bono, R. K., 2015, A Hadean to Paleoarchean geodynamo recorded by single zircon crystals: Science, v. 349, p. 521-524.

Wang, H., Weiss, B. P., Bai, X.-N., Downey, B. G., Wang, J., Wang, J., Suavet, C., Fu, R. R., and Zucolotto, M. E., 2017, Lifetime of the solar nebula constrained by meteorite paleomagnetism: Science, v. 355, p. 623-627.

Weiss, B., 2017, Paleomagnetism of the Jack Hills rocks and zircons, 2017 MagIC Workshop: Earth's Magnetic Field from the Beginning: La Jolla, CA, p. https://www.youtube.com/watch?v=kyxExXdlLpc&t=1213s.

Weiss, B. P., Maloof, A. C., Harrison, T. M., Swanson-Hysell, N. L., Fu, R. R., Kirschvink, J. L., Watson, E. B., Coe, R. S., Tikoo, S. M., and Ramezani, J., 2016, Reply to Comment on "Pervasive remagnetization of detrital zircon host rocks in the Jack Hills, Western Australia and implications for records of the early dynamo": Earth Planet. Sci. Lett., v. 450, p. 409-412.

Weiss, B. P., Maloof, A. C., Tailby, N., Ramezani, J., Fu, R. R., Hanus, V., Trail, D., Watson, E. B., Harrison, T. M., Bowring, S. A., Kirschvink, J. L., Swanson-Hysell, N. L., and Coe, R. S., 2015, Pervasive remagnetization of detrital zircon host rocks in the Jack Hills, Western Australia and implications for records of the early geodynamo: Earth Planet. Sci. Lett., v. 430, p. 115-128.